Self-Healable, Reprocessable, and 3D Printable Plant Oil-Based Elastomers and Facile Fabrication of Graphene Oxide Reinforced Copolymer Nanocomposites

by

Saadman Sakib Rahman

A thesis submitted in partial fulfillment of the requirements for the degree of

Master of Science

Department of Mechanical Engineering
University of Alberta

ABSTRACT

Prolonging service-life and durability of polymer-based products can help to reduce severe landfill/marine pollution caused by polymeric materials (i.e., elastomers and thermosets). Self-healing polymers are a class of polymers that are capable of healing cracks or mechanical damage inflicted upon them, with or without any external stimuli. Most of the self-healing materials reported in the literature are based on fossil fuels. As environmental regulations tighten up and industries are focused on making a transition from petroleum refinery to bio-refinery, a need arises to invent, develop, and market new bio-based products for advanced applications. However, it is challenging to synthesize self-healing polymers, especially thermosets and elastomers, from biomass, which are compatible with 3D printing technologies and can easily be reprocessed without degrading mechanical and thermal properties. On the other hand, polymeric materials usually display either high stretchability or high strength. In recent years, many studies have been conducted to resolve the long-standing conflict between strength and toughness, two vital and mutually exclusive mechanical properties, by incorporating nanofillers into the polymer matrices. Nonetheless, uniform dispersion of nanofillers to achieve strong matrix-filler interfacial bonding, which is essential for effective load transfer, is a major challenge in composite engineering.

This thesis reports the development of 3D printable, self-healing elastomers incorporating renewable components, and copolymer based nanocomposites for high performance applications.

In the first study, a self-healable, reprocessable, and inkjet 3D printable elastomer is reported, which is based on a diacrylate monomer synthesized from canola oil and a partially oxidized silicon-based copolymer containing free thiol-groups and disulfide bonds. In an inkjet 3D printing device, both substances are cross-linked via UV-irradiated thiol-ene-click chemistry. The self-healing and recycling attributes of the elastomer are achieved by phosphine-catalyzed disulfide

metathesis. The healed and reprocessed elastomers display mechanical properties and thermal stabilities comparable to the original, with self-healing and reprocessing efficiencies of ~86 and ~124%, respectively. Moreover, the elastomer shows excellent thermal stability before and after reprocessing. 5% weight loss temperature was found to be around 350 °C.

In the second part of this thesis, graphene oxide (GO) reinforced poly(styrene-*co*-methyl methacrylate) is synthesized via *in situ* bulk polymerization. The monomer ratios are optimized, and the effect of GO concentration on the mechanical and thermal properties of the copolymer are studied. The ultimate tensile strength, failure strain, and storage modulus of the copolymer were increased by 14.6, 15, and 43%, respectively, by adding only 0.1 weight fraction of GO. Furthermore, the thermal stability of the nanocomposites was better than the neat copolymer.

PREFACE

Parts of this thesis have been submitted or ready to be submitted for publication, as described below. Therefore, their structures are mostly maintained; i.e., each chapter has its introduction, methods, results, discussion, and abbreviations are defined at their first appearance. The bibliography is given in a separate chapter.

Chapter 2 will be submitted for publication as Rahman, S. S.; Arshad, M.; Qureshi, A.; Ullah, A., *Reprocessable and 3D printable self-healing bio-based elastomer using thiol-ene click chemistry and disulfide metathesis*. As the first author, I was responsible for concept formation, conducting the literature review, experiments, data analysis, and writing the manuscript. Dr. M. Arshad assisted in data collection and contributed to manuscript edits. Dr. Ahmed Qureshi and Dr. Aman Ullah are the supervisory authors and were involved in concept formation and revision of the manuscript.

Chapter 3 has been submitted for publication as Rahman, S. S.; Arshad, M.; Zubair, M.; Ghasri-Khouzani, M.; Qureshi, A., Ullah, A., *Facile fabrication of graphene oxide/poly(styrene-co-methyl methacrylate) nanocomposite with high toughness and thermal stability*. As the first author, I was responsible for concept formation, conducting the literature review, experiments, data analysis, and writing the manuscript. Dr. M. Arshad assisted in data collection and edited the manuscript. M. Zubair worked on graphene oxide synthesis and characterization part. Dr. M. Ghasri-Khouzani revised the draft of the manuscript. Dr. Ahmed Qureshi and Dr. Aman Ullah are the supervisory authors and were involved in concept formation and revision of the manuscript.

ACKNOWLEDGEMENTS

I would like to take this opportunity to express my deepest gratitude to my supervisors, Dr. Ahmed Qureshi and Dr. Aman Ullah, for guiding and motivating me through challenging tasks and helping me to grow as an independent researcher. I couldn't be more grateful to have them as my mentors on this academic journey.

I want to particularly thank Dr. Mohammad Arshad for helping me expand my knowledge in chemical synthesis, and for his help with the laboratory equipment and techniques that I have used throughout this research.

I am also grateful to my friends and wonderful colleagues in ADaMS Lab and Ullah's research group for insightful scientific discussions, and for their support and encouragement.

I would like to dedicate this thesis to my family and the memory of my grandparents: without their continuous support, inspiration, and motivation, none of this would have been possible.

CONTENTS

1. Introduction 1

1.1 Plastic pollution 1

1.2 Bio-based plastic 3

1.3 Self-healing polymers 4

1.4 3D printing 8

1.5 Polymer nanocomposite 9

1.6 Graphene oxide (GO) 9

1.7 Scope of the thesis 11

2. Reprocessable and 3D printable self-healing bio-based elastomer using thiol-ene click chemistry and disulfide metathesis 13

2.1 Introduction 13

2.2 Methods and characterization 16

2.2.1 Materials 16

2.2.2 Synthesis of canola oil methyl esters (COME) and its self-metathesis 17

2.2.3 Synthesis of dicarboxylic acid (9-Octadecene-1,18-dicarboxylic acid) 18

2.2.4 Synthesis of bis(2-(acryloyloxy)ethyl) octadec-9-enedioate (AEOD)[111, 112] 19

2.2.5 Synthesis of photopolymer ink 19

2.2.6 Inkjet 3D printing 19

2.2.7 Characterization 20

2.3 Results and discussion 23

2.3.1 Synthesis of AEOD monomer 23

2.3.2 Partial oxidation of MMDS 26

2.3.3 Fabrication and structural insight of the elastomer 27

2.3.4 Rheology of the ink 34

2.3.5 Mechanical properties, self-healing, and reprocessability 34

2.3.6 Thermomechanical properties and thermal stability 36

2.4 Conclusion 39

3. Facile fabrication of graphene oxide/poly(styrene-co-methyl methacrylate) nanocomposite with high toughness and thermal stability 40

3.1 Introduction 40
3.2 Materials and methods 42
3.2.1 Materials 42
3.2.2 GO synthesis 43
3.2.3 Copolymer synthesis 44
3.2.4 Preparation of polymer nanocomposites 44
3.2.5 Injection molding 45
3.2.6 Mechanical testing 45
3.2.7 Thermal analysis 46
3.2.8 Chemical and microstructural characterization 46
3.3 Results and discussion 47
3.3.1 Characterization of GO 47
3.3.2 Chemical and crystallographic analysis of nanocomposites 49
3.3.3 Microstructural characterization 51
3.3.4 Tensile testing 53
3.3.5 Thermomechanical analysis 58
3.3.6 Thermal transitions 60
3.3.7 Thermal stability 62
3.4 Conclusion 63
3.5 Acknowledgment 64
4. Conclusions and future work 65
4.1 Combined summary 65
4.2 Future directions 68
5. Bibliography 70

List of Tables

Table 2.1 Mechanical and thermal properties of the elastomer. 39

Table 3.1 M_w and PDI of the neat copolymer and GO reinforced polymer nanocomposites..... 51

Table 3.2 Ultimate tensile strength (UTS), ultimate strain, and Young's modulus values of the copolymer and GO reinforced nanocomposites..... 53

Table 3.3 T_g of the neat copolymer and GO reinforced nanocomposites measured by DSC and DMA techniques. 61

Table 3.4 Thermal degradation temperatures for 10, 50, and 90% weight loss of the neat copolymer and GO reinforced nanocomposites measured by TGA. 63

List of Figures

Fig. 1.1 The pathway by which plastic enters the world's oceans..... 2

Fig. 1.2 Global life-cycle GHG emissions of conventional plastics in 2015 by life-cycle stage and plastic type. 3

Fig. 1.3 Tributylphosphine catalyzed disulfide metathesis within a polysulfide network..... 5

Fig. 1.4 A timeline of landmarks for graphene synthesis and commercialization in the past decade. 10

Fig. 2.1 Self-metathesis of canola oil methyl esters (COME). *a*, *b*, *c* olefins. *d*, *e*, *f* monoesters. *g* diester. 18

Fig. 2.2 Photocrosslinking of MMDS with AEOD. (a) conversion of the diester to dicarboxylic acid and the reaction of the dicarboxylic acid with HEA, (b) Partial oxidation of MMDS using DIB, and (c) Thiol-ene addition reaction between AEOD and MMDS-disulfide oligomer..... 24

Fig. 2.3 Pictures of (a) dicarboxylic acid, (b) AEOD monomer, and (c) thiol-disulfide oligomers oxidized using different molar equivalent of DIB (at room temperature). (d) ^{1}H NMR of diester, diacid, and AEOD. (e) FTIR-ATR spectra of the diester, diacid, HEA, and AEOD. 25

Fig. 2.4 FTIR-ATR spectrums of MMDS partially oxidized using 0.3, 0.5, and 1.5 molar equivalent of DIB..... 27

Fig. 2.5 (a) FTIR-ATR spectra of MMDS, MMDS-OX, ink, and elastomer. (b) FTIR-ATR spectra of the ink and elastomer in the wavenumber range of 1600 to 1280 cm^{-1}. (c) DSC thermographs of AEOD, MMDS, and elastomer. (d) WAXRD spectrums of the original elastomer and after reprocessing..... 29

Fig. 2.6 Gel content (%) measurement. 30

Fig. 2.7 (a) Survey XPS scan of the elastomer. High-resolution deconvoluted XPS scans of (b) C 1s and (c) S 2p..... 31

Fig. 2.8 Inkjet 3D printing of reprocessable self-healing elastomer. (a) Inkjet 3D printing setup. (b) Demonstration of UV-curing after deposition. Photographs of (c) 3D printed dogbone, which is cut in half for a self-healing experiment, (d) and (e) after self-healing, (f) pieces that were used for reprocessing, (g) and (h) after reprocessing by compression molding. 33

Fig. 2.9 3D printed various shapes using a DLP system (Autodesk, Ember) and custom made tray. Irradiation time: 12 s..... 33

Fig. 2.10 (a) Rheological properties of the ink. (b) typical engineering stress-strain curves of the original, self-healed, and reprocessed samples. 36

Fig. 2.11 Thermomechanical properties of the elastomer. (a) The storage modulus (E') and loss modulus (E'') curves as a function of temperature. (b) The loss factor (tan δ) curve. Thermogravimetric analysis (TGA) of AEOD, MMDS, and the elastomer. (c) TGA curves and (b) the first derivatives of TGA curves. 37

Fig. 2.12 TGA thermograph of the reprocessed elastomer and its first derivative. (Increase in degradation temperatures could indicate an increase in crystallinity). 38

Fig. 3.1 (a) Illustration of the GO reinforced nanocomposites preparation. (b) Cryofractured GO (0.1) sample. (c) Injection-molded dogbones of pure copolymer and nanocomposites. 43

Fig. 3.2 Characterization of GO. (a) FTIR-ATR spectra of pristine graphite and GO. (b) WAXRD spectra of pristine graphite and GO. (c) as-synthesized GO. Typical TEM images of GO sheets in (d) water and (e) methanol solution. 48

Fig. 3.3 (a) FTIR-ATR spectra and (b) WAXRD profiles of the neat St(30):MMA(70) copolymer and GO (0.1) reinforced nanocomposite. 50

Fig. 3.4 TEM images of the cross-sections of (a) neat copolymer, (b) GO (0.075), (c) GO (0.1), (d) GO (0.25), (e) GO (0.5), and (f) GO (1) nanocomposites. AFM images of the solvent cast surface of GO (0.1) nanocomposite, in (g) tapping phase and (h) height sensor modes. 52

Fig. 3.5 (a) Representative tensile engineering stress-strain curves of the neat copolymer and GO reinforced nanocomposites at room temperature. (b) Comparison of the experimental Young's modulus of GO reinforced nanocomposites to values as calculated from Halpin-Tsai equations. 54

Fig. 3.6 SEM images of the cryofractured surfaces of (a) the neat copolymer, (b) 0.075, (c) 0.1, (d) 0.25, (e) 0.5, and (f) 1 wt.% GO reinforced nanocomposites. 58

Fig. 3.7 (a) Storage modulus and (b) damping or loss factor (tan δ) of the neat copolymer and GO reinforced nanocomposites as a function of temperature. 60

Fig. 3.8 DSC thermographs of the neat copolymer as well as GO reinforced nanocomposites... 60

Fig. 3.9 (a) TGA curves of the neat copolymer, GO, and GO reinforced nanocomposites. (b) DTG curves of the neat copolymer and GO reinforced nanocomposites. 62

1. Introduction

1.1 Plastic pollution

Oil and natural gas are the primary raw materials for plastic production. First, the raw materials are processed by a method known as 'cracking process,' which converts crude oil or natural gas components into hydrocarbon monomers, such as ethylene and propylene. Many units of these monomers are then chemically linked together to generate long polymer chains. Today, a world without plastics seems unimaginable, considering the extent to which plastics are used. Global production of plastics increased from 2 Mt in 1950 to 380 Mt in 2015.[1, 2] Though plastics made our daily lives more convenient, it is one of the major contributors to marine and environmental pollution. Most of the commonly used plastics are biodegradable therefore they accumulate in landfills, beaches, and oceans after their usual service-life. It has been estimated that by 2050, there will be more plastic waste in our oceans than fish.[3] As illustrated in Fig. 1.1, global plastic production was 270 Mt in 2010, whereas global plastic waste was 275 Mt.[4] In 2010, among the global annual plastic waste, around 8 Mt (3%) of plastics ended up in our oceans.[4] Thousands of marine animals get entangled in plastic rope and netting, abandoned fishing gear, plastic packaging waste every day. On the other hand, mircoplastics have been detected in the stomach of a range of marine lives, including plankton, seabirds, fishes, turtles, and whales. Ingestion of such plastic waste and entanglement in large plastic debris cause these species to die from internal injuries, starvation, and suffocation. Through consumption of seafood, mircoplastics can transfer to human bodies, which is identified as a health hazard. Pyrolysis and incineration are the only ways through

which plastic waste can be eliminated permanently; however, these processes are responsible for releasing more carbon into the atmosphere, fueling climate change.

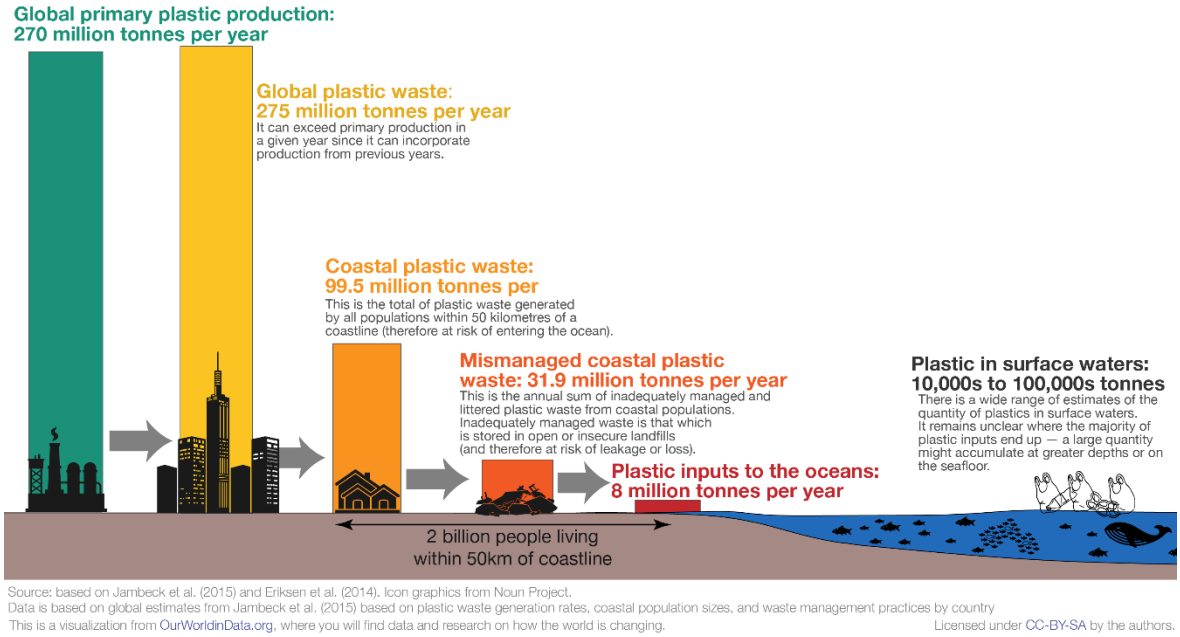

Fig. 1.1 The pathway by which plastic enters the world's oceans.[4]

Plastic end-of-life (EoL) processes such as incineration and pyrolysis are not the only source of greenhouse gas (GHG) emissions; plastic resin-production and conversion stages are, indeed, the principal contributors. Fossil fuel-based plastics produced in 2015 emitted 1.8 Gt CO_2-equivalent emissions over their life cycle, out of which the resin-production stage generated 61 percent and the conversion stage emitted 30 percent of total emission (Fig. 1.2).[5] To mitigate environmental pollution caused by plastics, an interdisciplinary approach is needed throughout the value chain. One strategy to tackle the problem is to gradually substitute fossil fuel-based plastics by bio-based plastics. Recycling and reuse of plastic materials are effective methods that could help to reduce accumulation of plastic debris in landfills, beaches, and oceans.

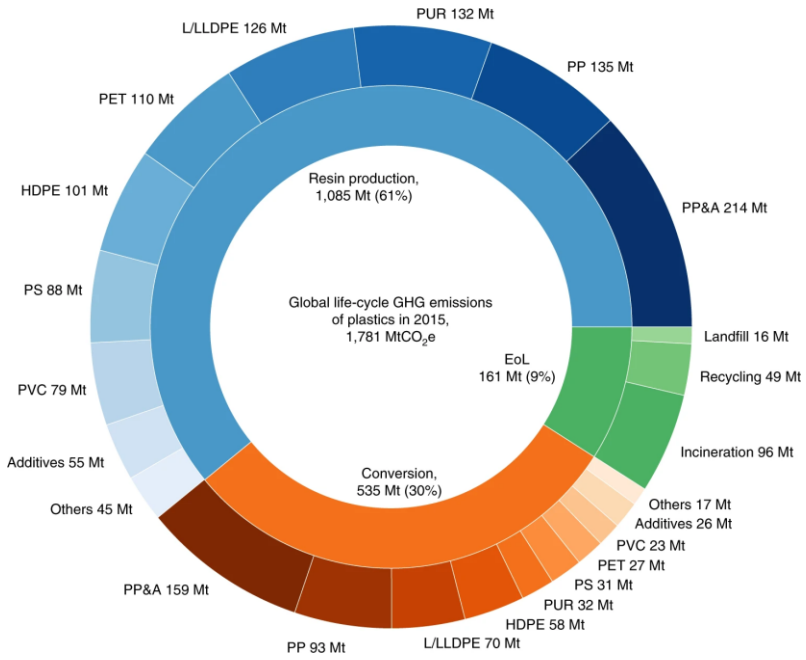

Fig. 1.2 Global life-cycle GHG emissions of conventional plastics in 2015 by life-cycle stage and plastic type.[5]

1.2 Bio-based plastic

Bio-based plastics refer to plastics that are made fully or partially from renewable biomass, such as plant oils, animal fats, starch, cellulose, sugars, proteins, instead of crude oil and gas. Life-cycle assessments have shown that bio-based plastics add less carbon to the atmosphere than petroleum-based plastics.[6] It has been reported that replacing 65.8% of world's fossil fuel-based plastics with bio-based plastics could reduce CO_2-equivalent emissions by 241-316 Mt per year.[7]

As a result of democratic geographic distribution, availability, and low-cost, plant oils are in a prominent position among other biomass. Plant oils consist of triglycerides, i.e., saturated and unsaturated fatty acid esters of glycerol. The polymers from renewable resources, including vegetable or plant oils have great potential to supplement and/or substitute petroleum based plastics.[8]

While bio-based plastics offer a multitude of sustainability-related benefits, there are some overarching challenges. For example, the processes of transforming biomass into useful monomers are often not so efficient and cost-effective. Some bio-based polymers do not show complementary or improved mechanical and thermal properties compared with the polymers available at present. Also, in some instances, industrial composting at high-temperature is necessary to degrade bio-based plastics.

1.3 Self-healing polymers

Natural biomaterials found in animals and plants have a unique ability to heal wounds. Inspired by nature, self-healing polymers, a type of smart materials that are able to restore their functionality after crack formation and other types of damage, have been developed in the last decade. Based on the approach of the healing mechanism, self-healing polymers can be divided in two groups: extrinsic and intrinsic. The extrinsic self-healing polymers contain microcapsules, microvascular networks, or hollow tubes, which upon damage release encapsulated healing agent (monomer) in the polymer matrix. Due to the capillary action and low viscosity, the healing agent or monomer eventually flow and cover the entire crack plane. A catalyst is usually embedded into the matrix to initiate polymerization of the monomer. When the monomer comes in contact with the catalyst, it solidifies and restores the damaged portion of the polymer. This process has been demonstrated through embedding dicyclopentadiene (DCPD) and Grubbs' catalyst in an epoxy matrix.[9] In recent years, different variation of this approach have also been studied and developed.[10]

Intrinsic self-healing systems, on the other hand, utilizes homolytic or heterolytic bond cleavage, dynamic covalent bonds or supramolecular chemistry. Intrinsic self-healing polymers often require an external stimuli, such as heat, pH, UV-light, etc., for the healing to take place. However, in contrast to the extrinsic type, these systems have the ability to perform multiple self-healing cycles

at the same place. This section highlights some of the major studies on the field of intrinsic self-healing polymers with a focus in dynamic disulfide bonds.

Li *et al.*,[11] fabricated polyurethane elastomer containing dynamic disulfide bonds, which exhibited self-healing efficiency of about 95% (based on tensile strength) after healing at 80 °C for 12 h. Canadell *et al.*,[12] used disulfide chemistry to introduce self-healing ability in a covalently cross-linked rubber. Epoxy resin containing disulfide bonds was cross-linked using tetrafunctional thiol. The self-healing test showed that the material can fully recover the original breaking strain when heated at 60 °C for 1 h. Additionally, it has been shown that a cross-linked epoxidized polysulfide can be self-healed with about 91% healing efficiency at room-temperature through phosphine-mediated disulfide metathesis reaction.[13] In contrast, aromatic disulfide metathesis can proceed at room-temperature without any help of a catalyst to yield quantitative healing efficiency. Fig. 1.3 illustrates the tributylphosphine (TBP) catalyzed disulfide metathesis reaction mechanism of the polysulfide network. Phosphine salt cationic intermediates and thiolate anions are formed in the initial step by the nucleophilic attack of TBP to the disulfide bonds. Then, the thiolate anions attack other sulfur atoms of the cationic intermediates, leading to exchanges of network chains.

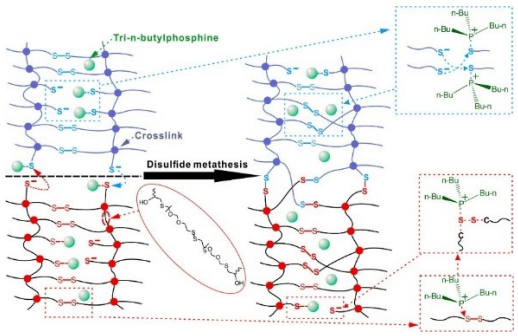

Fig. 1.3 Tributylphosphine catalyzed disulfide metathesis within a polysulfide network. Reprinted with permission from Ref. [13] Copyright (2014) American Chemical Society.

Yu *et al*.,[14] developed a self-healing elastomer by crosslinking thiol-disulfide oligomers of [4–6%(mercaptopropyl)methylsiloxane]-dimethylsiloxane (MMDS) with a vinyl-terminated polydimethylsiloxane (V-PDMS). The self-healing attribute was obtained through phosphine-mediated disulfide metathesis reaction. Though the elastomer exhibited 100% self-healing efficiency, tensile strength was relatively low (~16 kPa). It was also observed that incorporating disulfide linkages into the elastomer results in decrease in tensile strength. The study further provides the effect of disulfide content on the self-healing efficiency of the material. In another study, a silicone elastomer was fabricated by thiol-ene click reaction between V-PDMS and MMDS, followed by thermocuring between carboxyl and amido functionalized polysiloxanes.[15] The material not only exhibited self-healability with a self-healing efficiency of 98% at 100 °C (for 12 h), but also showed reprocessability with a recovery of 90% of the original tensile strength. Interestingly, thiol-ene click product of V-PDMS and MMDS (without any disulfide linkages) exhibited self-healing characteristic when exposed to sunlight.[16] However, no details on the self-healing efficiency of the elastomer was provided in the study. Additionally, the effect of the molecular weight of V-PDMS on the tensile properties of the elastomer was studied, which revealed that with the increase in molecular weight fracture strain of the elastomer increased significantly.

Ortiz *et al.*,[17] prepared a self-healing elastomer by photocrosslinking epoxy resin with a thiol-ene system, containing thiol-disulfide oligomers and a curing agent N^1, N^1, N^6, N^6-tetrallylhexane-1,6-diamine. At 60 °C temperature, ~8 h were required to achieve complete healing of the test specimen with 40 mol% of thiol-ene, while it took ~7 h for the test specimen with 50 mol% of thiol-ene. In addition, Xiang *et al.*[18] developed a self-healable and reprocessable elastomer via thiol-ene click reaction between the double bonds in polybutadiene and thiols in polysulfide. The self-healability and reprocessability features were achieved with the aid of UV-induced disulfide

metathesis. The sample recovered ~97% of the original shear strength when healed under UV irradiation (40 mW cm^{-2}) for 3 h.

The self-healable and recyclable polymeric materials can contribute to alleviate environmental challenges associated with the continuous increase in generation of plastic waste. In addition, self-healing elastomers have found applications in soft-robotics and wearable devices. Conventional soft robots are frequently damaged by sharp objects and edges present in the uncontrolled and unpredictable environments they operate in. Similarly, shear, wear, punctures, or overpressures can damage artificial muscles. Terryn *et al.*,[19] addressed such weaknesses by constructing a self-healing soft hand, a self-healing soft pneumatic gripper, and two self-healing pneumatic artificial muscles. The self-healing attribute of all three types of soft-robots is based on the Diels-Alder reaction between a diene (furan) and a dienophile (maleimide), and complete healing was obtained by heating the samples at 80 °C. A strain-sensitive, stretchable, and autonomously self-healable semiconducting film for fabrication of skin-like active-matrix strain sensor array was also developed, where the autonomous self-healing was achieved by metal-ligand coordination.[20] Tan *el al.*,[21] fabricated a self-healable, low-field illuminating optoelectronic stretchable light-emitting capacitor based on a poly(vinylidene fluoride)-based fluoroelastomer. The reversible non-covalent hydrogen-fluorine intermolecular bonds in the system gave rise to the repeatable self-healing capability. Ge *et al.*,[22] developed a self-healing hydrogel for strain and temperature sensor based on reversible metal-coordination, hydrogen bonding, and electrostatic interactions with ~90% self-healing efficiency in 6 h at room-temperature. More details on the self-healing materials for wearable devices can be found in the comprehensive review by Li *et al.*,[23]

Furthermore, there is a huge potential of self-healing hydrogels in therapeutic application.[24] The self-healability enables digital on demand drug release by initiating damage through ultrasound

pulses. Self-healing materials have also been used to develop 3D printed scaffolds.[25, 26] Fast moving space debris can cause catastrophic damage to a spacecraft through ballistic or hypervelocity impacts. To overcome such dangers of air and space travel, NASA scientists are now developing self-healing polymeric materials.[27-30]

To conclude, self-healing capacity of the polymeric materials can substantially reduce the need to perform inspection, troubleshooting, repair, and/or replacement of damaged parts. Furthermore, self-healing of minor damage can help increase service-life of plastic products, in turn, reduce plastic waste generation.

1.4 3D printing

Additive manufacturing or 3D printing is a process of making three dimensional solid objects from computer-aided design (CAD) models in a layer-by-layer manner.[31] 3D printing methods allow the rapid design and fabrication of objects with high level of geometrical complexities without the need for expensive tooling. Although the metal 3D printing technologies are in their inceptive stage, 3D printing methods that are exclusive to polymers, such as, stereolithography,[32] fused deposition modeling,[33] material jetting or inkjet 3D printing,[34, 35] direct ink writing[36] etc., already are well-developed.[37]

Material jetting or inkjet 3D printing process involves the deposition of photocurable inks on a substrate and polymerization by illumination with an ultraviolet (UV) light source. Droplet formation is a critical issue in any inkjet 3D printing system, which directly controls the surface roughness, mechanical properties, and dimensional tolerance of the 3D printed parts. Drop formation mainly depends on the dispensing device, including the velocity of the ejected droplet and the nozzle diameter, as well as the ink's viscosity, surface tension, and characteristic droplet

length.[38] These parameters must all be tightly controlled to achieve good print quality. The in-house developed inkjet 3D printer used in this thesis, consists of a gantry type motion platform, a printing head, a pressure-driven dispensing system, a UV-light source, a motion control module, digital and analog Input/Output modules, and a power supply. The details of the printer can be found in Ref.[39].

1.5 Polymer nanocomposite

Polymer nanocomposite is a type of composite material where nanofillers (spheres, rods, plates) are dispersed in a polymer matrix in an effort to expand the functionality and use of the polymer by significantly improving its performance properties.[40] The addition of nanomaterials or nanofibers in polymer matrices often results in superior mechanical and thermomechanical properties,[41, 42] increased thermal and electrical conductivities,[43, 44] better electromagnetic interference shielding,[45] improved gas-barrier,[46] etc., as compared to the virgin polymers and micro-particle reinforced polymer composites. Such improvements are mainly due to the large interfacial area between polymers and nanofillers, load transfers from polymer matrix to significantly tougher and stronger nanofillers, decrease in polymer chain mobility, tortuosity, and formation of continuous networks of nanofillers to produce conductive paths. Graphene,[47] graphene oxide (GO),[48] carbon nanotubes,[49] cellulose nanocrystals,[50] montmorillonite,[51] silver nanoparticles,[52] gold nanorods[53] are some of the commonly used nanofillers in the literature.

1.6 Graphene oxide (GO)

Andre Geim and Konstantin Novoselov won the Nobel Prize in 2010 for their groundbreaking experiments on graphene.[54, 55] Since then, graphene became a heated topic of research (Fig. 1.4). Graphene is a flat monolayer of carbon atoms tightly packed into a two-dimensional honeycomb lattice. It is the strongest material ever measured with record thermal and electrical conductivities.[56-

[58] In the last decade, graphene has been one of the most widely used nanofillers for polymer nanocomposites. However, graphene sheets have strong tendency to agglomerate and form clusters due to strong interactions between the sheets thus, the dispersion of graphene in a polymer matrix is a very challenging task. Nonetheless, one key property of graphene is that it can be readily chemically functionalized by epoxy, hydroxyl, carbonyl, carboxylic acid, etc. Graphene oxide (GO) is a form of graphene functionalized by oxygen-containing groups.[59-61] The oxygenated-groups attached to the basal plane and edges of graphene sheets help to achieve better interfacial interaction with the polymer matrix, without sacrificing the benefits offered by unmodified graphene. As a result, in the recent years, GO based polymer nanocomposites have already found applications in aerospace and automobile,[62-64] sensors,[65-67] energy storage,[68, 69] packaging,[70-73] biomedical,[74-77] and, so on.

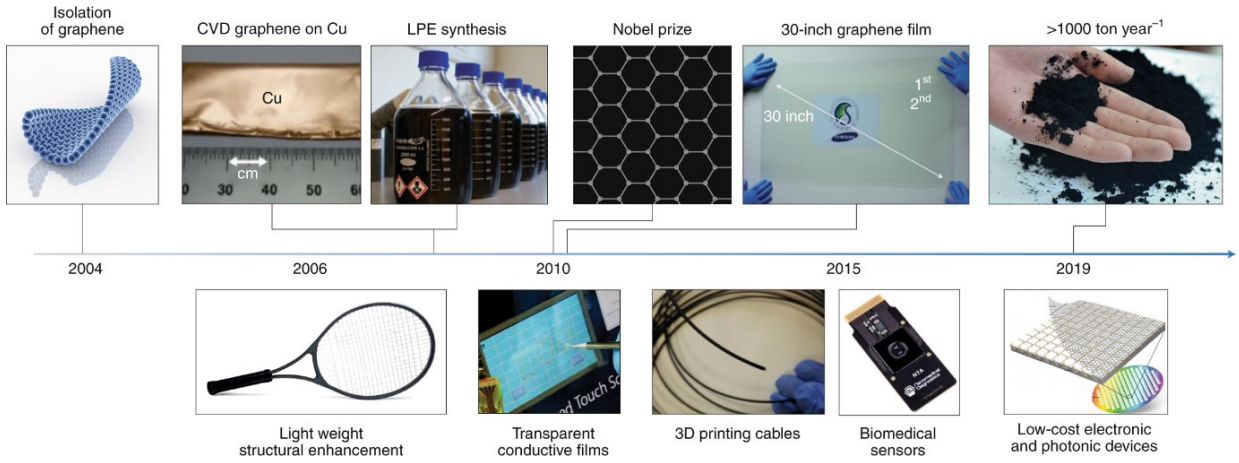

Fig. 1.4 A timeline of landmarks for graphene synthesis and commercialization in the past decade. Reprinted with permission from Ref.[78] Copyright (2019) Springer Nature.

1.7 Scope of the thesis

Self-healing polymers have attracted considerable research attention in recent years. There are also few reports in the literature on recyclable thermosets and elastomers. The advent of 3D printing technologies has provided new methods for the synthesis of such smart materials. However, most of the studies reported in the literature on self-healing and recyclable elastomers are focused on petrochemical-based monomers.

In this thesis, motivated by the environmental challenges we face today, a partially bio-based elastomer is developed, which has the ability of self-healing and can also be reprocessable and 3D printable. The chemical structure, mechanical, thermomechanical, and thermal properties of the elastomer are studied and reported in **Chapter 2**.

Extension of service-life and durability of the existing thermoplastics can also reduce global plastic consumption to an extent. Unfortunately, strength and toughness, two vital mechanical properties, are mutually exclusive. Nanofillers, especially graphene and its derivatives, have shown promise to enhance the strength and toughness of polymeric materials. However, uniform dispersion of nanofillers in copolymer matrices to attain strong matrix-filler interfacial bonding, which is essential for effective load transfer, is the least investigated aspect and a major challenge in composite engineering.

Chapter 3 investigates the effect of GO concentration on poly(styrene-co-methyl methacrylate) matrix with the aim of increasing the mechanical and thermal properties of the copolymer. First, the monomer ratio of the copolymer was optimized based on the mechanical properties. The GO reinforced copolymer nanocomposites were then prepared by an *in situ* bulk polymerization. Injection moldability of the material was also demonstrated. The mechanical, thermomechanical, and thermal properties were studied. Crack arresting mechanism and dispersion state of GO sheets

in the copolymer matrix were also investigated using scanning and transmission electron microscopes. This study provides an understanding of the dispersion morphology of GO in a copolymer matrix. It was found that using an optimized concentration of GO, mechanical and thermal properties of the copolymer can be substantially improved.

In **Chapter 4**, an overall conclusion and future perspectives for each chapter is provided.

2. Reprocessable and 3D printable self-healing bio-based elastomer using thiol-ene click chemistry and disulfide metathesis

2.1 Introduction

Plastic pollution has become a global crisis in today's world as it not only contributes to climate change but also severely pollutes our oceans and kills thousands of marine animals every year. In 2018, worldwide production of plastics reached 359 million tonnes, which is expected to double in the next 20 years.[79-81] Thermosets and elastomers (occupy roughly half of the total plastic market) are generally non-biodegradable and cannot be reused or recycled thus, after their service-life, they linger in the environment for a long time. If plastic waste is incinerated, it releases dangerous gases into the atmosphere, which can fuel global warming. This is not the only source of emissions of dangerous gases, tons of greenhouse gases are emitted during the extraction and conversion of oil and natural gas into plastic raw-materials. It has been reported that fossil fuel-based plastics produced in 2015 emitted about 1.8 Gt CO_2-equivalent emissions over their life cycle.[5] One strategy to tackle this problem is to gradually substitute fossil fuel-based plastics by bio-based plastics. Recycling or reprocessing of thermosets and elastomers, on the other hand, is an effective method that could help to reduce accumulation of plastic debris in landfills, beaches, and oceans.

Bio-based plastics refer to plastics that are made fully or partially from renewable biomass, such as plant oils, animal fats, starch, cellulose, sugars, proteins, instead of crude oil and gas. Life-cycle assessments have shown that bio-based plastics add less carbon to the atmosphere than petroleum-based plastics.[6] As a result of democratic geographic distribution, availability, and low-cost, plant

oils are in a prominent position among other biomass.[82] Nevertheless, the processes of transforming plant oils into useful monomers are often not so efficient and cost-effective. More research work focused on the development of innovative technologies of transforming biomass, especially plant oils, into novel polymeric materials are required to utilize the abundant renewable resources fully.

Self-healing is one of the essential biomaterial characteristics that improves survival and lifetime for most plants and animals. Inspired by wound healing in nature, polymeric materials have been developed that can heal cracks and other types of damage inflicted on them, and able to recover their original functionalities.[83-86] Introducing self-healing attribute can substantially reduce the need to perform inspection, troubleshooting, repair, and/or replacement of damaged parts. Furthermore, self-healing of minor damage can help increase the service-life of any plastic products which, in turn, will reduce plastic waste generation to an extent. As a result of all these benefits, self-healing polymers have already found applications in various fields, including soft-robotics,[24, 87] flexible electronics,[23] space engineering,[88] controlled drug-delivery,[89] biomedical devices,[90] coatings,[91] and so on.

Self-healing mechanisms can typically be broken up into two principal groups: extrinsic and intrinsic self-healing. Extrinsic self-healing mechanism is achieved by loading microcapsules or hollow fibers containing healing agent and appropriate catalyst in a polymer matrix.[10] As this mechanism requires additional additives to be embedded in the matrix, mechanical properties of the extrinsic self-healing polymers are lower as compared to their virgin polymer. The irreversible nature of this mechanism is yet another limitation. Intrinsic self-healing polymers,[92] on the other hand, can be healed multiple times due to the presence of dynamic covalent bonds[93] such as Diels-Alder bonds,[94] dynamic disulfide bonds,[13] reversible B-O bonds,[95] or non-covalent bonds, for

example, hydrogen bonds,[96] π–π stacking interactions,[97] host-guest interactions,[98] metal-ligand interactions[99], etc.

Disulfide bond has attracted increasing attention recently due to its reasonable level of bond strength, moderate reaction conditions, and the ability to break and reform spontaneously at room temperature or in response to multiple stimuli, including heat, light, and pH.[11, 12, 13] Moreover, disulfide bonds can easily be formed through oxidation of thiols.[100] In a recent study, Yu *et al*.,[14] fabricated a self-healing elastomer through crosslinking a vinyl-terminated polydimethylsiloxane with thiol-disulfide oligomers of [4–6%(mercaptopropyl)methylsiloxane]-dimethylsiloxane. The elastomer reported in the study exhibited 100% self-healing efficiency however, tensile strength was relatively low (~16 kPa). Though self-healing elastomers are studied extensively in recent years, most of the studies reported in the literature used petrochemical-based monomers. Only a few reports on the synthesis and fabrication of fully or partially bio-based self-healing elastomers.

Photoinitiated thiol-ene addition reactions[101, 102] combine the classical benefits of click chemistry with the advantages of a photoinitiated process, making it an ideal candidate as a cross-linking mechanism in the field of stereolithography (SLA),[103, 104] digital light processing (DLP),[15, 105, 106] and material jetting or inkjet 3D printing[34, 35] systems. Thiol-ene based resins have several advantages over (meth)acrylate-based formulations for example, reduced oxygen inhibition, lower shrinkage stress, delayed gel point, simplified polymer kinetics, and higher biocompatibility.[107]

Inkjet 3D printing is an additive manufacturing process that involves the deposition of liquid photocurable inks in the form of droplets or continuous lines to print layers on top of each other, and successive curing of the deposited layers via UV or light irradiation. Thiol-ene click chemistry can be utilized to synthesis new materials that can be fabricated through inkjet 3D printing systems. Although several reports on thiol-ene based resins for DLP and SLA systems have been published,

only a few studies were conducted on synthesis and development of thiol-ene based inks for inkjet 3D printing systems. Furthermore, 3D printing of self-healing elastomers that exhibit stress and strain recovery via self-healing is in its infancy.[11, 14, 15, 108] To the best of our knowledge, there are no reports on the fabrication of bio-based self-healable and reprocessable elastomer by inkjet 3D printing utilizing thiol-ene click reaction and disulfide metathesis.

Herein, we report a novel partially bio-based, self-healing, fully recyclable, and 3D printable elastomer. A diacrylate monomer synthesized from canola oil and a partially oxidized silicon-based copolymer were cross-linked via a combination of UV irradiation (free-radical thiol-ene addition) and phosphine-mediated thiol-Michael addition in an inkjet 3D printing system. Self-healing and reprocessing features were attained through dynamic disulfide metathesis, assisted by a phosphine catalyst at elevated temperature. Mechanical, thermomechanical, thermal, and chemical properties of the elastomer were thoroughly analyzed. The self-healing and recycling efficiencies were determined from uniaxial tensile tests. The elastomer reported here can be a viable green replacement for fossil-oil based materials in applications such as soft-robotics, flexible wearable electronics, and biomedical devices. In addition, recyclability feature of the elastomer will help to mitigate plastic waste generation and marine pollution. Furthermore, this work will inspire the development of novel 3D printable fully or partially bio-based elastomers that have both the self-healing and recycling attributes.

2.2 Methods and characterization

2.2.1 Materials

Canola oil, potassium hydroxide (≥85%), methanol (99.8%), Hoveyda-Grubbs catalyst 2nd generation (HG2, 97%), ethyl acetate (EtOAc, ≥99.5%), silica gel (high-purity grade, average pore size 60 Å, 70-230 mesh), tetrahydrofuran (THF, ≥99.9%), sodium hydroxide (≥98%), diethyl ether

(≥99.0%), sodium sulfate (Na_2SO_4, ≥99.0%), 4-(dimethylamino)pyridine, (DMAP, ≥99%), dichloromethane (DCM, ≥99.8%), dicyclohexylcarbodiimide (DCC, 99%), 2-hydroxyethyl acrylate (HEA, 96%), thin-layer chromatography (TLC) plates, (diacetoxyiodo)benzene (DIB, 98%), tributylphosphine (TBP, 97%), phenylbis(2,4,6 trimethylbenzoyl)phosphine oxide (BAPO, Irgacure 819, 97%), and toluene (99.8%) were purchased from Sigma-Aldrich. Hydrochloric acid (HCl, 36.5 to 38.0%), sodium chloride (NaCl, ≥99.0%), and sodium bicarbonate ($NaHCO_3$, ≥99.7%) were purchased from Fisher Scientific, and n-hexane (95%) was purchased from Caledon. [4-6% (mercaptopropyl)methylsiloxane] – dimethylsiloxane (MMDS) copolymer was supplied by Gelest. All chemicals, unless otherwise stated, were used as received.

2.2.2 Synthesis of canola oil methyl esters (COME) and its self-metathesis

Transesterification of canola oil into COME was performed according to the previously reported method.[109] As an example, 2.5 g KOH was dissolved in 80 mL of methanol and added to 300 g of canola oil in a 1 L reaction flask. The mixture was stirred rapidly at ambient temperature for 6 h, and the formed glycerol (bottom layer) was removed. 1.25 g KOH in 40 mL of methanol was then added to the upper layer and stirred for 4 h to ensure complete transesterification of canola oil. The upper layer was separated, washed with distilled water (4 × 1 L), and passed through a silica gel column to get purified COME with 82% yield. The self-metathesis of COME was performed on a customized microwave reactor at 50 °C for 30 min using the HG2 catalyst (0.05 mol%) under a nitrogen environment.[110] The self-metathesis product was characterized using GC-MS, GC-FID, and TLC, and the desired component dimethyl-9-octadecene-1,18-dioate (diester) was separated via silica gel column chromatography using an eluent system of 1-5% v/v EtOAc in n-hexane. (Schematic is shown in Fig. 2.1)

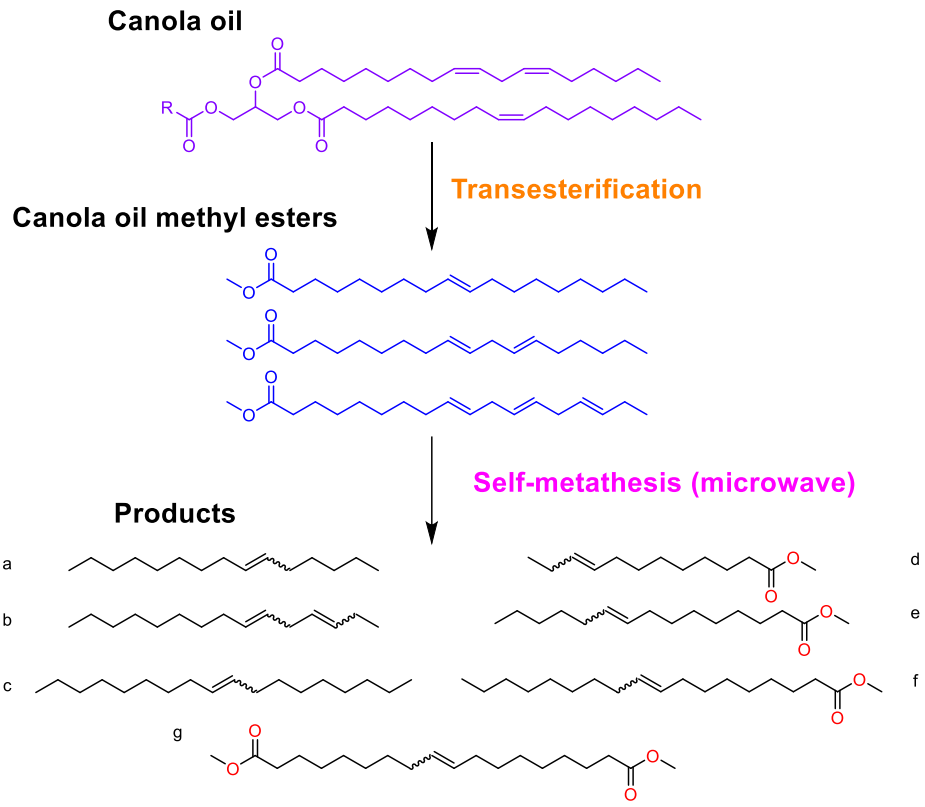

Fig. 2.1 Self-metathesis of canola oil methyl esters (COME). *a*, *b*, *c* olefins. *d*, *e*, *f* monoesters. *g* diester.

2.2.3 Synthesis of dicarboxylic acid (9-Octadecene-1,18-dicarboxylic acid)

Typically, in a round-bottom flask equipped with a magnetic stirrer and a reflux condenser, diester (10 g, 29 mmol) was dissolved in THF (500 mL), and NaOH (aq., 4N, 500 mL) was added to the solution. The resulting immiscible mixture was stirred rapidly and refluxed for 24 h at 75 °C. The reaction was then cooled down to room temperature and transferred to a separation flask. The aqueous layer was separated and acidified to pH = 2 by adding 20 N HCl. The precipitate was extracted with diethyl ether (750 mL), washed with brine solution (750 mL), and the organic phase was dried with Na_2SO_4. Removal of solvent under vacuo afforded 8.1 g of white solids (yield: 89%; Fig. 2.2a and 2.3a).

2.2.4 Synthesis of bis(2-(acryloyloxy)ethyl) octadec-9-enedioate (AEOD)[111, 112]

In a 1 L round-bottomed flask, above synthesized dicarboxylic acid (10 g, 32 mmol) and DMAP (0.782 g, 6.401 mmol) were dissolved in dry DCM (500 mL). The reaction flask was placed on an ice-water bath, stirred, and purged with nitrogen for 15 min. In a separate beaker, DCC (13.86 g, 67.2 mmol) was dissolved in a minimum volume of DCM, and the solution was transferred into the reaction flask. HEA (7.8 mL, 67.2 mmol) was then added drop-wise to the reaction mixture with the help of a syringe in 15 min. The ice-water bath was removed after 30 min, and the resulting solution was stirred for 24 h at ambient temperature (the reaction progress was monitored by TLC). After complete consumption of the starting material, the insoluble solids were filtered off, and the filtrate was washed with distilled water (500 mL) respectively, saturated solution of $NaHCO_3$ (500 mL), and brine solution (500 mL). The organic phase was dried with anhydrous Na_2SO_4, and the solvent was removed in vacuo to retrieve 11.87 mL product (yield: 74%; Fig. 2.2a and 2.3b).

2.2.5 Synthesis of photopolymer ink

As a standard example, 0.23 g (0.715 mmol) of DIB was dissolved in 4 mL of toluene. In a separate vial, MMDS (10 g, 1.429 mmol) was taken and the prepared DIB solution was added into it. The mixture was stirred vigorously for 5 min. Later, AEOD (1.09 g, 2.144 mmol), BAPO (0.17 g, 1.5 wt.%), Sudan-I (6 mg, 0.05 wt.%), and TBP (8 µL) were added to the vial under continuous magnetic stirring. The ink formulation was stirred for an additional 10 min to ensure the uniformity of the mixture and ultrasonicated for 3 min to degas. (Fig. 2.2b and c)

2.2.6 Inkjet 3D printing

3D printing was carried out on a custom inkjet 3D printer fitted with a high precision dispenser (Ultimus V, Nordson EFD) and a UV-LED source (CBT-120, Luminus). The details of the printer are published elsewhere.[39] Parts were printed in a layer-wise fashion with a rectilinear infill pattern

using a 0.5 mm diameter needle. The exposure time was 120 s for each layer, and the layer thickness was ~0.3 mm. After printing, specimens were thoroughly rinsed with isopropyl alcohol, the sides were trimmed to dimensions required to attain testing standards, and dried in an oven for 2 h at 60 °C.

2.2.7 Characterization

The proton nuclear magnetic resonance (^{1}H NMR; 400 MHz, chloroform-d, 26.9 °C) spectra were acquired on a Varian INOVA instrument. FTIR-ATR (Fourier Transform Infrared Spectroscopy-Attenuated total reflectance) tests were conducted on a Bruker Alpha FTIR spectrophotometer (Bruker Optics). For each sample, 16 scans at a resolution of 4 cm^{-1} over the range of 410−4000 cm^{-1} were collected. The rheological experiments were performed on an Advanced Rheometer AR 2000 (TA instruments) by the cone (40 mm, 2°) and plate geometry. The flow curve was fitted with the Cross model (Eqn. 2.1). The Herschel-Bulkley equation (Eqn. 2.2) was used to model the shear stress versus shear rate curve and to determine the yield stress of the photocurable ink, which is the shear stress at zero shear rate.

$$\frac{\eta - \eta_\infty}{\eta_o - \eta_\infty} = \frac{1}{1 + (K\dot{\gamma})^m} \tag{2.1}$$

$$\tau = \tau_o + C\dot{\gamma}^n \tag{2.2}$$

Where η is the viscosity, η_o is the zero shear viscosity, η_∞ is the infinite shear viscosity, K is the Cross constant, m is the shear thinning index, τ is the shear stress, $\dot{\gamma}$ is the shear rate, τ_o is the yield stress, C is the consistency index, and n is the flow index.

Wide Angle X-ray Diffraction (WAXRD) analysis was performed on Ultima IV (Rigaku) fitted with a Cu-kα (λ = 1.5406 Å) source. The samples were scanned from 4° to 60° (2θ) with 0.02 step size and 2° min^{-1} scanning time using the standard stage. X-ray Photoelectron Spectroscopy (XPS)

experiments were performed using Kratos Axis (Ultra) spectrometer equipped with an Al-Kα (hν = 1486.71 eV) X-ray source at a pass energy of 160 eV (survey scan) or 20 eV (high-resolution scan). Charge effects were corrected by using C 1s peak at 284.8 eV. A Shirley background was applied to subtract the inelastic background of high-resolution peaks and the peaks were deconvoluted through the peak components represented by a 30% Gaussian—70% Lorentzian function. Uniaxial tensile tests of the samples (ASTM D638 Type V standard) were carried out on a high-precision Shimadzu Autograph AGS-X instrument at a cross-head speed of 10 mm min^{-1}. At least three samples were tested for each condition at room temperature, and the mean values and the standard deviations were reported. The viscoelastic properties of the elastomer were characterized using dynamic mechanical analysis (DMA). The tests were performed in the tension film mode on a Q800 DMA (TA Instruments), equipped with a liquid-nitrogen cooling apparatus. Samples with a dimension of 15 mm × 8 mm × 0.9 mm were tested at a frequency of 1 Hz. The temperature was first equilibrated at −150 °C and then increased at a heating rate of 2 °C min^{-1} to 25 °C. The glass transition temperature (T_g) was determined from the peak of the loss factor (tanδ) curve. Differential scanning calorimetry (DSC) analysis was conducted on a Q100 DSC (TA instruments) by heating the samples in the range of −90 to 50 °C at a heating ramp of 5 °C min^{-1}. Thermogravimetric analysis (TGA) was performed on a Q50 TGA (TA Instruments) at a heating rate of 10 °C min^{-1} from 25 to 600 °C under a nitrogen atmosphere. The gel content of the elastomers, both printed and recycled, was calculated from Eqn. 2.3.[113] The samples were first weighed before being soaked in toluene for 72 h, followed by drying in a vacuum oven at 80 °C for 4 h. Cross-linking density (v_e) of the elastomer was estimated using Eqn. 2.4 as reported in literature.[114]

$$Gel\ content\ (\%)\ = \frac{w_2}{w_1} \times 100 \tag{2.3}$$

$$v_e = \frac{E_o}{3RT} \tag{2.4}$$

Where, w_1 and w_2 are the weights measured before and after equilibrium swelling. E_o is the storage modulus in the rubbery plateau region (T_g + 40 °C), R is the gas constant, and T is the absolute temperature.

A razor blade was used to cut the samples in half, and the damaged interfaces were back in contact immediately by applying a slight pressure from both ends, followed by heating at 80 ° C for 8 h. The stress-strain curves of the healed samples were obtained from uniaxial tensile testing. The 3D printed specimens used for tensile testing were cut into small pieces and hot-pressed at 120 °C for 30 min, and 110 °C for 1 h under a compression force of 32 MPa. The reprocessed thin-film was cooled down to room temperature and annealed in a heating oven at 60 °C for 12 h before trimming according to the ASTM D638 Type V standard for uniaxial tensile testing.

2.3 Results and discussion

2.3.1 Synthesis of AEOD monomer

The schematic representation for the synthesis of the novel canola-oil based diacrylate monomer (AEOD) is shown in Fig. 2.2a. AEOD was synthesized using the following four steps: (i) transesterification of canola oil and self-metathesis of COME, (ii) extraction and purification of dimethyl-9-octadecene-1,18-dioate (diester), (iii) conversion of the diester to 9-Octadecene-1,18-dicarboxylic acid (dicarboxylic acid), and (iv) the coupling of the dicarboxylic acid with HEA. The findings and thorough discussion of the first two steps were previously published elsewhere.[115] Dicarboxylic acids are generally known to be more reactive than their diesters. In this study, the conversion of the diester to the dicarboxylic acid in high purity and quantitative yield was achieved through base-catalyzed ester hydrolysis using NaOH in THF solvent at elevated temperature. ^{1}H NMR and FTIR-ATR analysis of the product substantiates the successful conversion of the diester to the dicarboxylic acid. As can be seen in ^{1}H NMR spectra of the diester (Fig. 2.3d), methoxy ester protons (labeled as ***a***) appeared as a singlet at chemical shift (δ) of 3.65. After ester hydrolysis, ***a*** signal disappeared from the spectra of the dicarboxylic acid, indicating a successful conversion. In the FTIR-ATR spectra of the dicarboxylic acid (Fig. 2.3e), the characteristic sharp carbonyl (C=O) stretching band of diester at 1738 cm^{-1} shifted to an intense carboxylic acid C=O stretching band at 1687 cm^{-1}. The strong and broad absorbance band centered at about 2900 cm^{-1}, overlapping C-H stretch, is ascribed to carboxylic acid hydroxyl (O-H) stretching vibration. Furthermore, medium carboxylic acid O-H bending vibration peaks also appeared around 1432 and 913 cm^{-1}. These results confirm successful hydrolysis of diester into dicarboxylic acid.

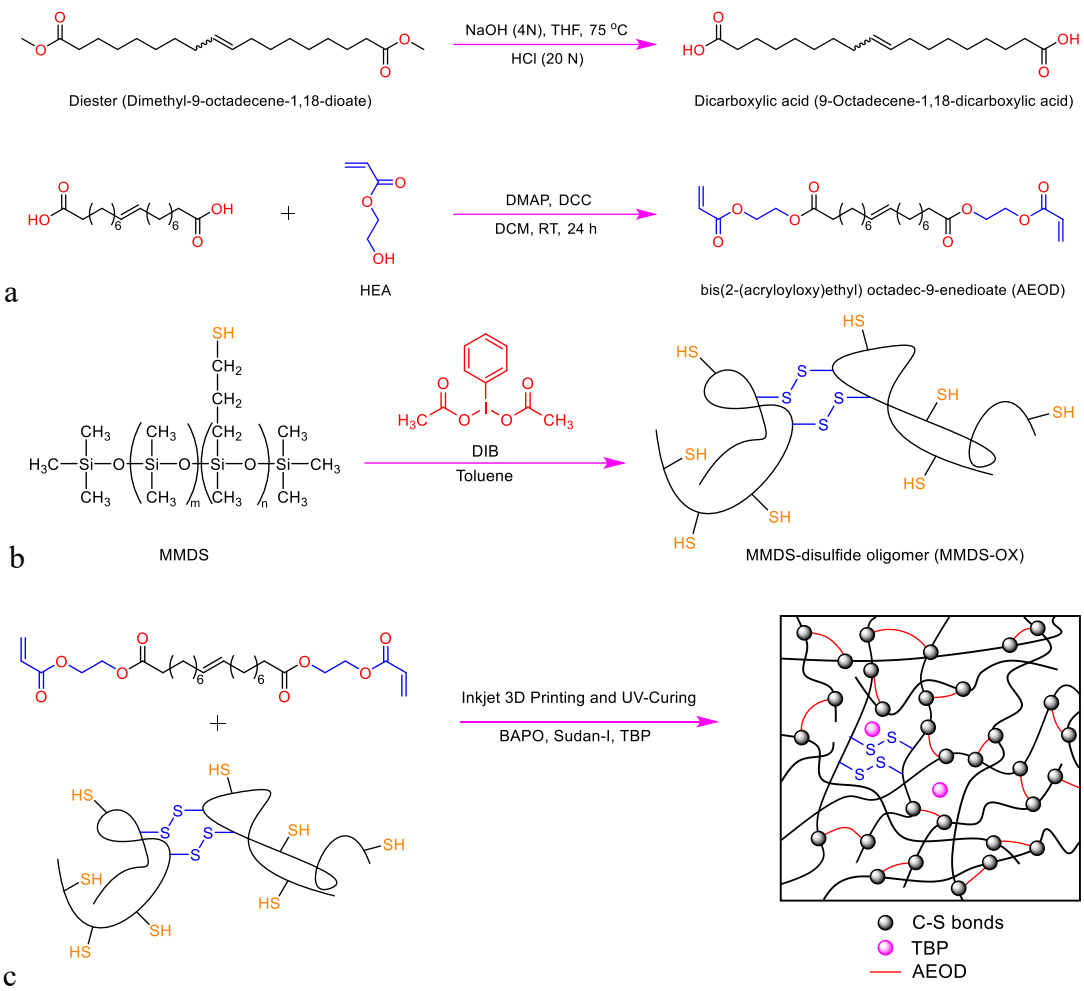

Fig. 2.2 Photocrosslinking of MMDS with AEOD. (a) conversion of the diester to dicarboxylic acid and the reaction of the dicarboxylic acid with HEA, (b) Partial oxidation of MMDS using DIB, and (c) Thiol-ene addition reaction between AEOD and MMDS-disulfide oligomer.

AEOD monomer was prepared by condensation of the dicarboxylic acid with HEA in the presence of DCC as a coupling agent and DMAP as a catalyst in DCM solvent. The structure of the product was verified by ^{1}H NMR (Fig. 2.3d). Along with the signals related to the dicarboxylic acid protons, additional signals ascribed to acrylic protons in between δ 4.51-6.45 ppm (labeled as $\boldsymbol{H_a}$, $\boldsymbol{H_b}$, and $\boldsymbol{H_c}$) and ethylene protons (marked as $\boldsymbol{g}$) appeared in the ^{1}H NMR spectrum of AEOD

monomer. Additionally, the reaction product was also analyzed by FTIR-ATR, as shown in Fig. 2.3e. No peaks related to the alcohol O-H stretching vibration band centered at 3433 cm^{-1} and carboxylic acid O-H band centered about 2900 cm^{-1} were detected in the spectra of AEOD, which indicates that the terminal O-H groups of HEA and dicarboxylic acid were entirely consumed after the condensation reaction. Moreover, the appearance of the C=C stretching band at 1636 cm^{-1} and diester C=O stretching band at 1728 cm^{-1} further confirms the successful coupling of HEA with the dicarboxylic acid.[116]

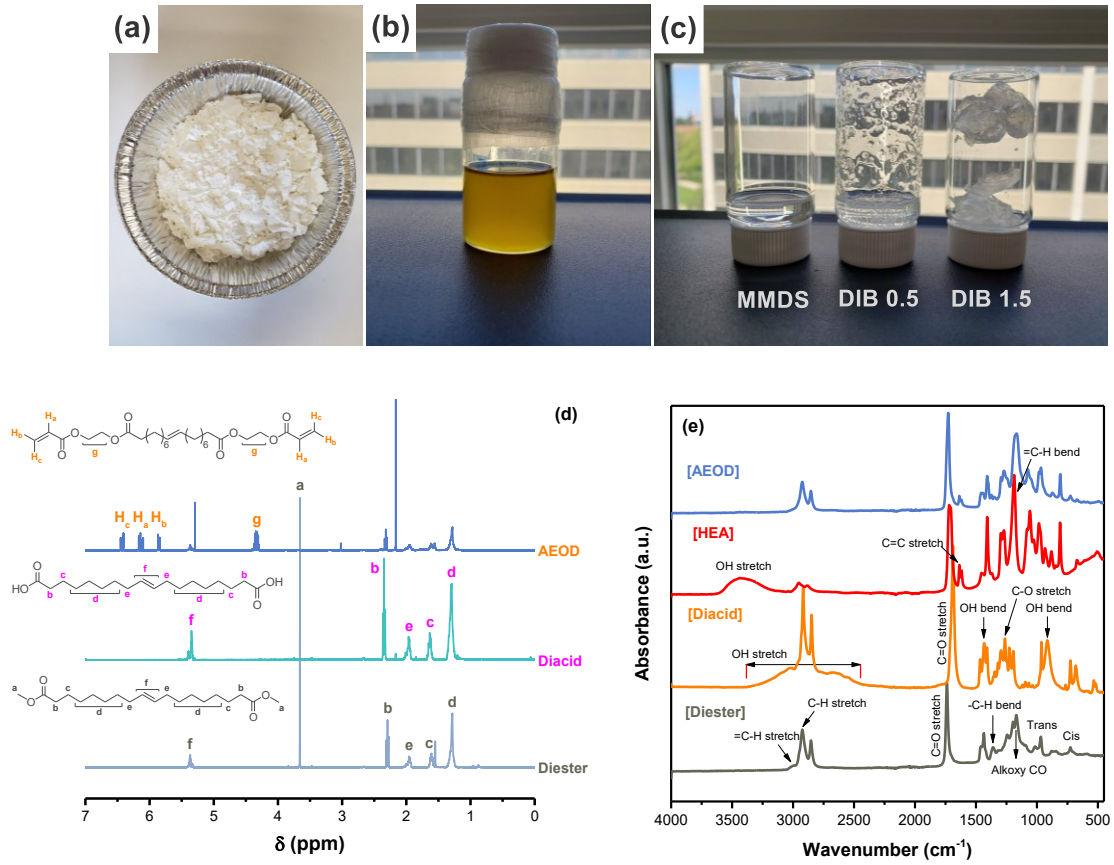

Fig. 2.3 Pictures of (a) dicarboxylic acid, (b) AEOD monomer, and (c) thiol-disulfide oligomers oxidized using different molar equivalent of DIB (at room temperature). (d) ^{1}H NMR of diester, diacid, and AEOD. (e) FTIR-ATR spectra of the diester, diacid, HEA, and AEOD.

2.3.2 Partial oxidation of MMDS

To introduce dynamic disulfide bonds, we partially oxidized the thiol-containing copolymer (MMDS) before photocrosslinking with AEOD (Fig. 2.2b). The conversion of thiols to disulfide bonds mainly depends on the type and concentration of the oxidizing agent. DIB has been shown to facilitate rapid oxidation of thiols at room temperature in two steps.[100] In the first step, the formation of sulfenyl iodide intermediate takes place through ligand exchange between DIB and thiol, followed by ligand exchange of a second thiol molecule with sulfenyl iodide intermediate to form a disulfide bridge and iodobenzene by-product. Three equivalents (0.3, 0.5, and 1.5 eqv.) of DIB in toluene were screened, and the resulting oxidized products were analyzed by FTIR-ATR. As shown in Fig. 2.4, the weak absorbance band around 463 cm^{-1}, attributed to the disulfide bond,[17, 117-119] were found to increase when DIB concentration was increased. Complete oxidation of MMDS was observed in the case of 1.5 eqv. of DIB, which led to the formation of insoluble polydisulfide (see Fig 2.3c). Thiol-disulfide oligomer obtained from the partial oxidation of MMDS using 0.5 eqv. of DIB (MMDS-OX) was selected for further analysis and ink preparation.

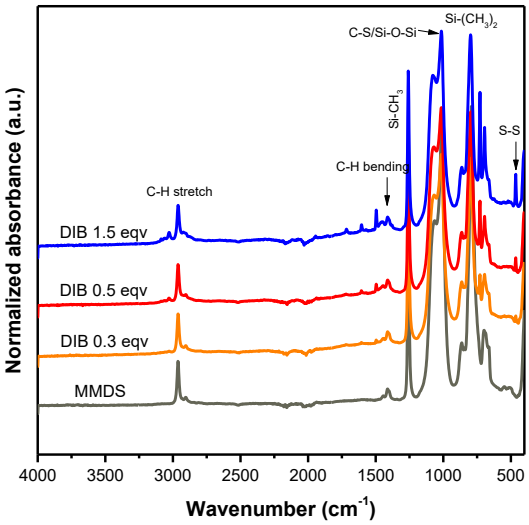

Fig. 2.4 FTIR-ATR spectrums of MMDS partially oxidized using 0.3, 0.5, and 1.5 molar equivalent of DIB.

2.3.3 Fabrication and structural insight of the elastomer

Radical-mediated (photochemically or thermally) thiol-ene reactions begin by forming a thiyl radical through hydrogen atom abstraction from a thiol compound. The formed thiyl radical then performs an anti-Markovnikov addition to the C=C bond yielding an intermediate carbon-centered radical followed by a chain transfer step with a second thiol compound to produce the corresponding thioether product and a new thiyl radical.[120] Thiol-ene systems that involve a thiol compound and an α,β-unsaturated electron-deficient alkene (e.g., acrylates) proceed by both homopolymerization of the alkene monomer as well as the step-growth polymerization.[121] In such cases, the intermediate carbon-centered radical is capable of adding across another C=C bond in addition to the usual chain transfer reaction.[122] This chain-growth results in the formation of oligomers or homopolymers in the final product. Besides, electron-deficient alkenes are more suitable for the thiol-Michael addition, which also has all the benefits of click chemistry, and can

readily be accomplished using a mild base or a nucleophilic (amines or phosphines) catalyst in a very low amount.[123]

Although thiol-ene addition reactions can be initiated without the use of a photoinitiator, a Type-I photoinitiator (BAPO) was used in our ink formulation as it provides up to four radicals and extended absorption window (360 to 440 nm),[124] which are advantageous for the 3D printing operation. The ink composition further comprises a phosphine catalyst TBP at extremely low amount. It has been reported in the literature that TBP can catalyze the thiol-Michael addition to provide the corresponding thioether adducts with quantitative yields,[125] and can also assist the disulfide metathesis.[13, 14] In our ink formulation, it is likely that cross-linking initiates by the conjugate addition of TBP to an activated C=C bond forming a phosphonium-enolate zwitterionic intermediate, which deprotonates the thiol to generate a thiolate anion.[126] Thiolate anion then undergoes direct conjugate addition to an activated C=C bond yielding a carbanion intermediate. The deprotonation of an additional thiol by the carbanion produces the desired thiol-Michael product. It is expected that the presence of the phosphine catalyst in the ink formulation could reduce the chain growth of the C=C bond to an extent as a result of the thiol-Michael addition.[126] The reaction rate of the thiol-Michael addition is directly dependent on the concentration of TBP. When higher than 15 μL of TBP was added in the mixture, it took less than 30 minutes for the reaction to complete. No observable reactants remained by the time the reaction mixture could be transferred to the inkjet 3D printing system. Therefore, initial qualitative trials were made to determine the amount of TBP that results in a moderate reaction rate. This enabled us to perform the primary cross-linking via UV-irradiated thiol-ene addition during the inkjet 3D printing operation.

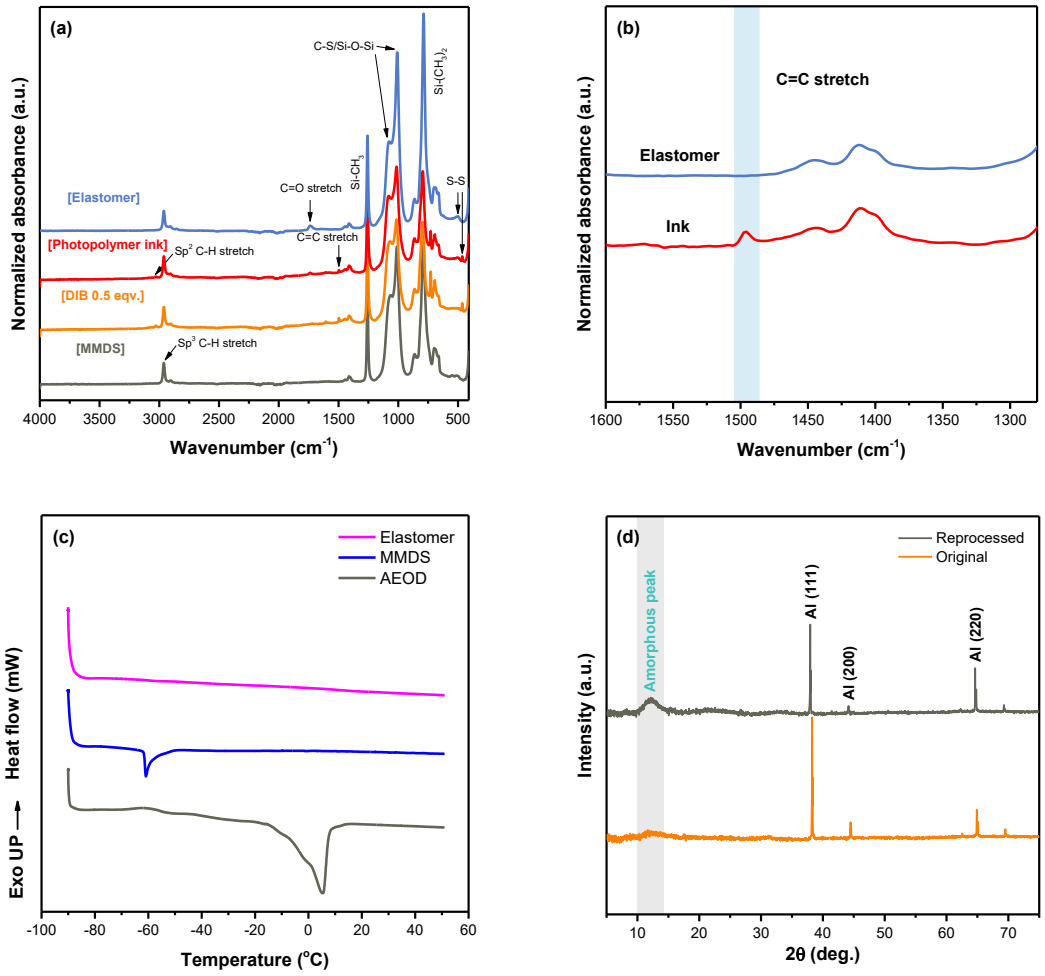

Fig. 2.5 (a) FTIR-ATR spectra of MMDS, MMDS-OX, ink, and elastomer. (b) FTIR-ATR spectra of the ink and elastomer in the wavenumber range of 1600 to 1280 cm^{-1}. (c) DSC thermographs of AEOD, MMDS, and elastomer. (d) WAXRD spectrums of the original elastomer and after reprocessing.

FTIR-ATR spectrums of the photocurable ink and cross-linked elastomer are shown in Fig. 2.5a. The low-intensity peak at 1734 cm^{-1} is ascribed to the ester C=O stretching band, and the sharp absorbance peaks at 1256, 1007, and 787 cm^{-1} are attributed to the Si-CH_3, C-S stretch/Si-O-Si, and Si-$(CH_3)_2$ bonds, respectively.[127] Moreover, the disulfide bond peak has shifted from 463 to 501 cm^{-1} after UV-curing. This result indicates a formation of a cross-linked structure consisting

of AEOD and MMDS-OX. The characteristic peak of the Si-CH_3 bond was selected as a standard for normalizing the spectrums to analyze the degree of conversion of the C=C bond. As illustrated in Fig. 2.5b (wavenumber: 1600 to 1280 cm^{-1}), the C=C stretching vibration peak at 1495 cm^{-1} disappeared from the spectrum of the elastomer, indicating complete consumption of the C=C bonds after 3D printing. Gel content percentage of the elastomer was determined to be 89%, which also proves that a high curing extent was achieved. The portion of the elastomer, where the density of cross-linking is low, dissolved in toluene; however, the highly cross-linked region swelled and formed a gel, as shown in Fig. 2.6.

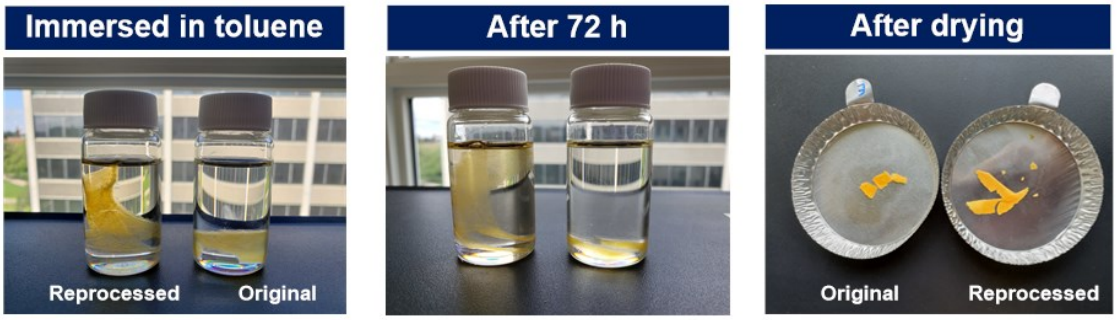

Fig. 2.6 Gel content (%) measurement**.**

DSC traces of AEOD, MMDS, and the elastomer are shown in Fig. 2.5c. The melting temperatures of AEOD and MMDS are around 5 and -60 °C, respectively. No endothermic melting peak of AEOD and MMDS can be detected in the DSC thermograph of the elastomer, indicating the formation of a cross-linked amorphous structure. The noncrystalline or amorphous nature of the elastomer was further confirmed by WAXRD analysis (Fig. 2.5d). As can be seen in the WAXRD spectra of the elastomer, a weak amorphous halo appeared at around $2\theta = 12°$ however, no crystalline peaks related to the material can be indexed (note that the sharp peaks at $2\theta = 38$, 45, and 65° are from the aluminum sample holder).

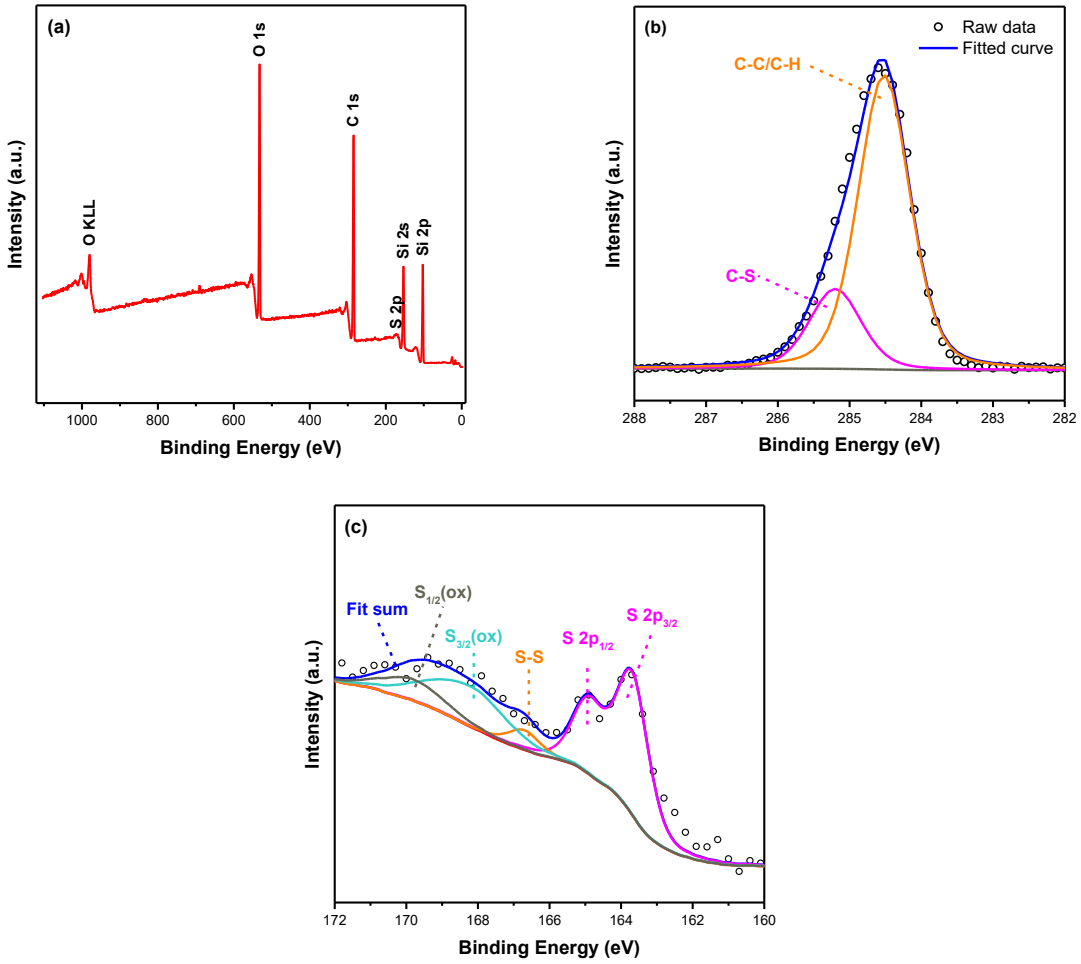

Fig. 2.7 (a) Survey XPS scan of the elastomer. High-resolution deconvoluted XPS scans of (b) C 1s and (c) S 2p.

The elemental composition of the elastomer was determined by the XPS survey spectra. Peaks related to O 1s, C 1s, Si 2s, Si 2p, and S 2p were detected in the survey spectra as shown in Fig. 2.7a. Bonding states of C and S can be studied more clearly through high-resolution XPS C 1s and S 2p spectrums. The high-resolution XPS C 1s spectra exhibited two peaks located at 284.5 and 285.2 eV binding energies after deconvolution, which are ascribed to C-C/C-H and C-S bonds, respectively (Fig. 2.7b).[128] Deconvoluted XPS S 2p spectra, as shown in Fig 2.7c, consists of a spin-orbit split doublet peak and three singlet peaks. The doublet peaked at 163.7 eV, is assigned

to S $2p_{3/2}$ and S $2p_{1/2}$ states of the C-S covalent bonds.[128-131] The peak positioned at 166.7 eV in the S 2p spectrum is attributable to the S-S bonds.[128] These observations, also supported by the FTIR-ATR results, confirm the presence of both the C-S and S-S bonds on the elastomer. Additionally, two peaks from the oxidized-sulfur species were identified at higher binding energies (167.9 and 169.8 eV).[129] This could be due to oxidation of unreacted thiols on the sample surface as a result of their storage in air, or there is a possibility that during oxidation in the presence of DIB solution some thiols have been converted to sulfur oxides. Moreover, the intensities of the $S_{3/2}$(ox) and $S_{1/2}$(ox) peaks are equal or slightly higher than the S-S peak, mainly because XPS only detects ionized electrons from atoms located up to a depth of several nanometers.

In this study, we cross-linked MMDS-OX and AEOD in an inkjet 3D printing system. One layer of the ink was deposited on the build-plate, and then the deposited layer was UV-cured for 120 s followed by the deposition of the second layer and subsequent curing (Fig. 2.8a and b). Though we were able to print multiple layers, good dimensional accuracy was not achieved due to the limitation of the printer. Nonetheless, dimensional accuracy can be improved by optimizing the printing parameters through Design of Experiments (DoE).[132] To further highlight the printability of our material, we printed different shapes using a DLP system[133] (see Fig. 2.9).

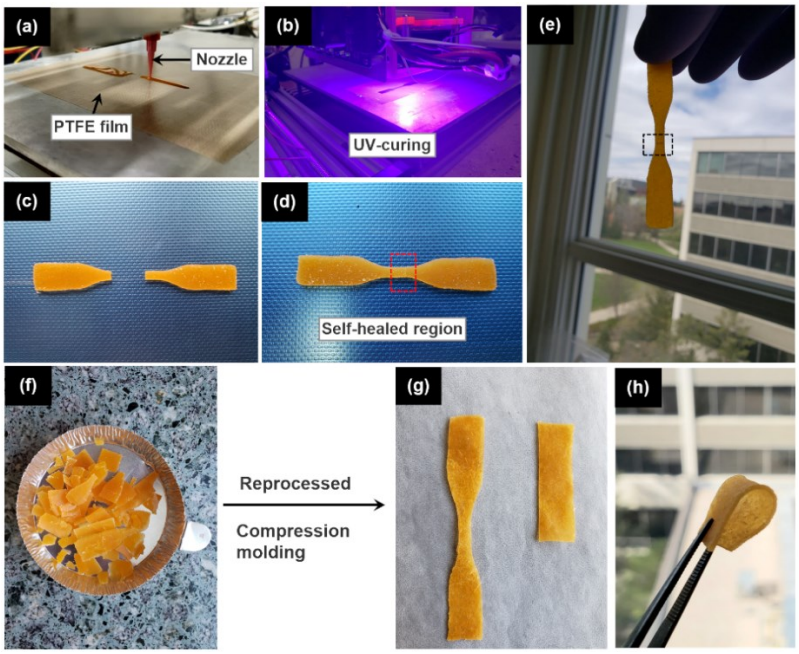

Fig. 2.8 Inkjet 3D printing of reprocessable self-healing elastomer. (a) Inkjet 3D printing setup. (b) Demonstration of UV-curing after deposition. Photographs of (c) 3D printed dogbone, which is cut in half for a self-healing experiment, (d) and (e) after self-healing, (f) pieces that were used for reprocessing, (g) and (h) after reprocessing by compression molding.

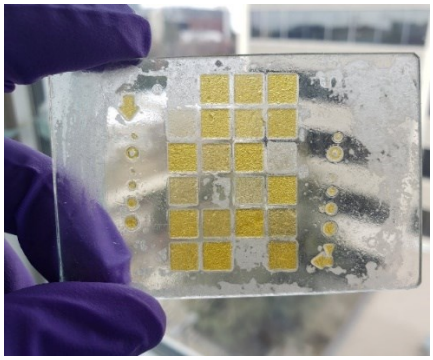

Fig. 2.9 3D printed various shapes using a DLP system (Autodesk, Ember) and custom made tray. Irradiation time: 12 s.

2.3.4 Rheology of the ink

Ink rheology is one of the most crucial parameters of an inkjet 3D printing system. The viscosity (η) of the ink under applied shear stress (τ) should be low enough to enable successful extrusion and formation of droplets.[36, 134] Fig. 2.10a shows η of our ink formulation as a function of shear rate ($\dot{\gamma}$). According to the Cross-model, the zero shear viscosity (η_o), which is η at near-rest conditions, was determined to be 37.73 Pa.s. However, a significant drop in η is observed as $\dot{\gamma}$ increased, and the infinite shear viscosity (η_∞) and shear thinning index (m) were estimated to be 1.45 Pa.s and 0.82 (the value of m ranges from 0 for Newtonian to 1 for infinite shear thinning). The low η and η_∞ values allowed the ink to be printable at room temperature without any solvents or diluents. Additionally, to approximate the stress under which the elastic structure breaks down (yields) and the ink starts to flow, a shear stress ramp was carried out (Fig. 2.10a). The yield stress (τ_o) and flow index (n) were determined by fitting τ versus $\dot{\gamma}$ curve with the Herschel-Bulkley model. The values of τ_o and n were found to be 2.64 Pa and 0.79, respectively, and n value lower than unity further confirms the ink's shear thinning behavior.

2.3.5 Mechanical properties, self-healing, and reprocessability

To provide insight on the mechanical strength and elasticity of the elastomer presented in this work, uniaxial tensile tests were performed, and typical engineering stress-strain curves of the original, self-healed, and reprocessed samples are provided in Fig. 2.10b. The original sample can be stretched up to 24.2 ± 0.28% with a tensile strength of 51.9 ± 0.1 kPa and Young's modulus of 0.23 ± 0.01 MPa. To demonstrate self-healing ability, 3D printed dogbones were cut into two separate pieces with a razor blade (Fig. 2.8c), and freshly damaged interfaces were brought in contact with a gentle compressive force (~0.08 N). After healing at 80 °C for 8 h (Fig. 2.8d and e), we performed uniaxial tensile tests on the samples to determine the self-healing efficiency from

the ratio of breaking strain of the healed sample to that of the original one. The healed sample recovered ~100% of the original tensile strength (52.3 ± 8.1 kPa) and ~86% of the breaking strain (20.8 ± 3.6%). In case of a control sample that does not contain disulfide bonds, no self-healing effect was observed. Thus, the self-healing process is mainly attributed to the disulfide metathesis reaction, accelerated by the phosphine salt catalyst, TBP. The nucleophilic attack of TBP to a disulfide bond generates a thiolate anion and TBP cationic intermediate. The cross-nucleophilic attack of the thiolate anion at another sulfur atom of cationic intermediate then leads to the reshuffling of disulfide bonds in the networked structure and reformation of the catalyst to its initial state, which, in turn, repeats the process.[13, 17, 135] As indirect evidence of free thiols was observed in the XPS S 2p spectrum, it is likely that these free thiols, if any, undergo thiol-disulfide exchange reaction[136-139] and therefore, contributes to the self-healing process in a way.

Conventional elastomers contain chemically cross-linked permanent networks, so they cannot be reprocessed and reshaped by melting or dissolving in a solvent. In the literature, however, it has been reported that the presence of dynamic covalent bonds facilitates the reprocessing and reshaping of cross-linked thermosets and elastomers.[13, 15, 108] Here, we have further demonstrated the self-healability of our elastomer through thermal reprocessing or recycling (Fig. 2.8f-h). Remarkably, not only did the reprocessed elastomer recover the original tensile strength and stretchability, but it also displayed slightly better mechanical properties than the original sample. For the reprocessed sample, tensile strength and breaking strain were 58.5 ± 4.3 kPa and 30 ± 0.8%, respectively (Fig. 2.10b). This difference could result from a decrease in the cross-linking density, as evidenced by the measured gel content (83%) value and an increase in the crystallinity due to the realignment of chemically cross-linked networks after compression molding, as evidenced by the WAXRD spectrum (Fig. 2.5d).

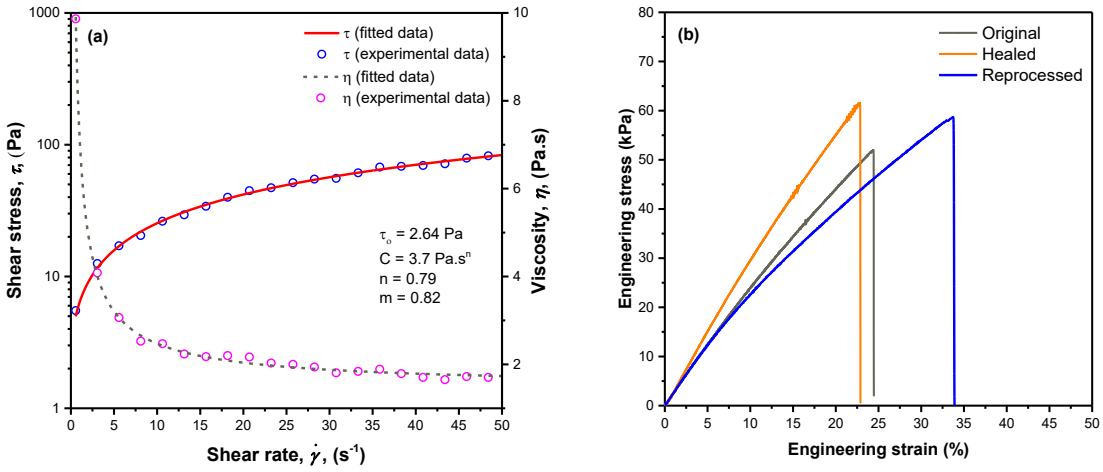

Fig. 2.10 (a) Rheological properties of the ink. (b) typical engineering stress-strain curves of the original, self-healed, and reprocessed samples.

2.3.6 Thermomechanical properties and thermal stability

DMA testing was performed to determine the viscoelastic properties and T_g of the elastomer. Fig. 2.11a displays a typical storage modulus (E')/loss modulus (E'') vs. temperature curve, where E' is a measure of the elastic response and E'' is the viscous response of the elastomer. The sample showed a clear transition from glass plateau to rubbery plateau, with E' dropping from ~4076 to 0.32 MPa. T_g can usually be determined from the damping or loss factor (tan δ) peak. As shown in Fig. 11b, the elastomer shows a T_g of -115.2 °C, which is in accordance with the values reported in the literature of silicon-based elastomers.[15, 104, 113] Using Eqn. 2.4 and E' value at T_g + 40 °C, the cross-linking density of the elastomer was calculated to be 6.26×10^{-5} mol cm^{-3}, suggesting a high degree of cross-linking.[113, 114]

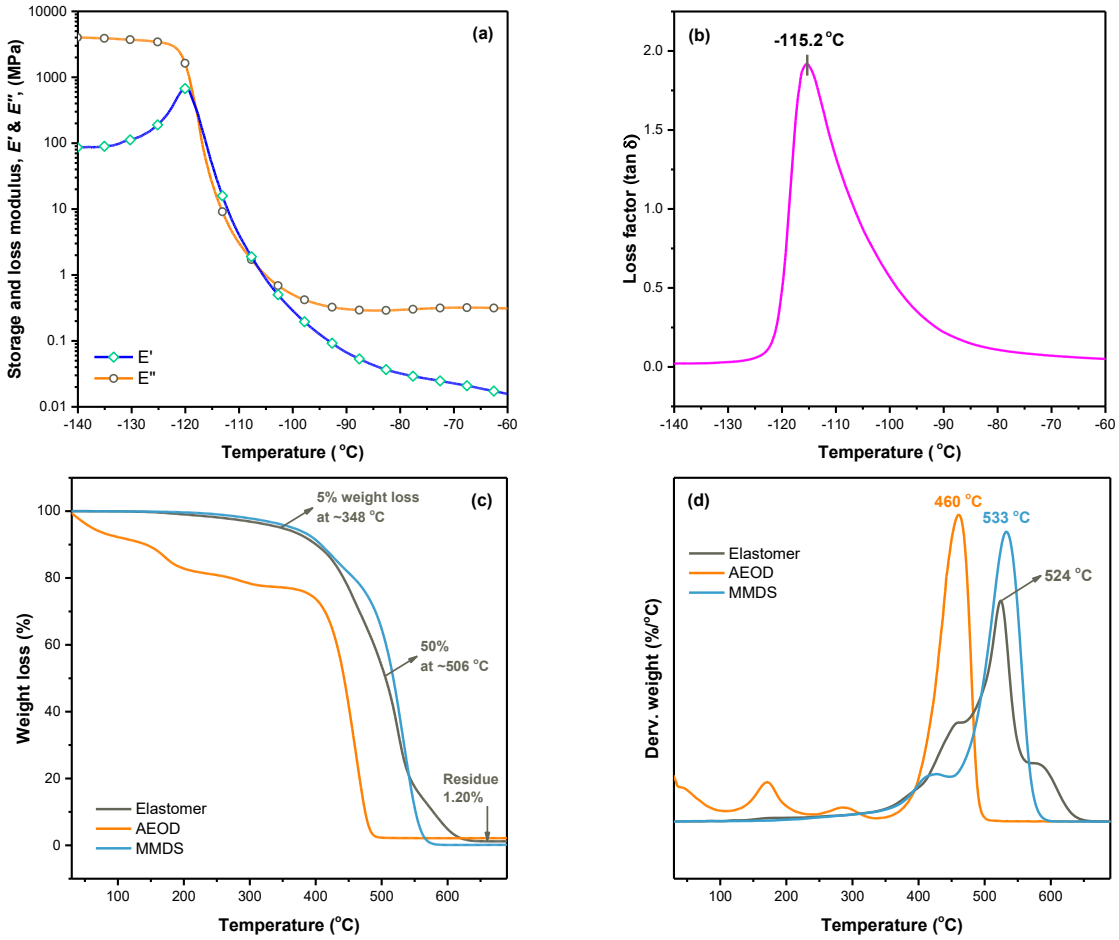

Fig. 2.11 Thermomechanical properties of the elastomer. (a) The storage modulus (*E′*) and loss modulus (*E″*) curves as a function of temperature. (b) The loss factor (tan δ) curve. Thermogravimetric analysis (TGA) of AEOD, MMDS, and the elastomer. (c) TGA curves and (d) the first derivatives of TGA curves.

The thermal stabilities of AEOD, MMDS, and the elastomer were investigated through TGA and its first derivative, and the results are plotted in Fig. 2.11c and d. AEOD exhibits an initial weight loss stage at 169 °C, which is probably due to the evaporation of bound moisture. The second (285 °C) and final (460 °C) stages are related to the degradation of the functional groups of AEOD and its primary structure. MMDS, on the other hand, displayed a two-stage degradation

as indicated by the weight-loss stages at 428 and 533 °C, resulting from the depolymerization, decomposition, and random scission of the copolymer chains. Three distinct mass-loss stages were observed in the case of elastomer. The first stage (around 461 °C) is primarily attributed to the cleavage of the C-S bonds[118] and, in turn, the evaporation of AEOD from the cross-linked network. While the second stage (524 °C) is caused by the degradation of MMDS. The minor weight-loss stage at the higher temperatures could be associated with the homolytic cleavage of the S-S bonds, and subsequent evaporation of the organosulfur compounds.[118, 140] The residue obtained after heating the sample to 700 °C could be mostly residual char and sulfur.[141] Overall, the elastomer exhibited excellent thermal stability (even after reprocessing, Fig. 2.12). Table 2.1 provides the overview of the mechanical and thermal properties of the reported elastomer.

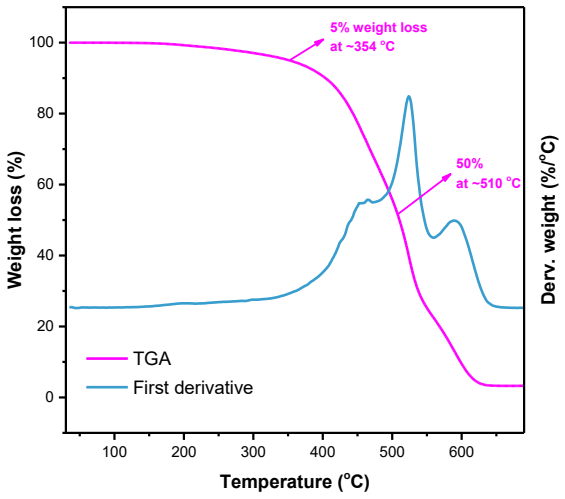

Fig. 2.12 TGA thermograph of the reprocessed elastomer and its first derivative. (Increase in degradation temperatures could indicate an increase in crystallinity).

Table 2.1 Mechanical and thermal properties of the elastomer.

T_g (°C)	UTS (kPa)	Breaking strain (%)	Young's modulus (kPa)	Self-healing efficiency	Reprocessing efficiency	$T_{d5\%}$ (°C)
-115.3	51.9 ± 0.1	24.2 ± 0.28	231 ± 1.6	~86%	~124%	~348

2.4 Conclusion

In summary, we report a novel elastomer that is partially bio-based (from canola oil) and is not only capable of self-healing but also completely reprocessable. Utilizing thiol-ene click chemistry, the elastomer was cross-linked in an inkjet 3D printing system. The self-healing feature was attained by introducing dynamic disulfide bonds on the cross-linked network, which can undergo a disulfide metathesis reaction with the aid of a phosphine catalyst. The healed and reprocessed elastomers display mechanical properties and thermal stabilities comparable to the original, with self-healing and reprocessing efficiencies of ~86 and ~124%, respectively. It is noteworthy that the elastomer reported herein has relatively high elasticity and low strength. However, mechanical strength and toughness can be improved by incorporating a cyclic compound (ring compound) in AEOD or through epoxidation of the unsaturated bond. Moreover, it is also possible to use a different thiol-containing monomer with a rigid structure. The strategy demonstrated in this work has the potential to mitigate petroleum oil consumption and to substantially reduce plastic waste that has caused severe environmental and marine pollution. Finally, considering the 3D printability, self-healability, and flexibility, this elastomer should find applications in soft-robotics, flexible electronics, and biomedical devices.

3. Facile fabrication of graphene oxide/poly(styrene-co-methyl methacrylate) nanocomposite with high toughness and thermal stability

3.1 Introduction

Graphene is a flat monolayer of carbon atoms tightly packed in a two-dimensional honeycomb lattice.[54] A great deal of effort has been made to develop lightweight, durable, and tough graphene-reinforced composite materials owing to the exceptional physical properties of graphene, for instance, Young's modulus near 1 TPa and almost 100 times greater tensile strength (130 GPa) than steel,[56] thermal conductivity above 3000 $Wm^{-1}K^{-1}$,[57] complete impermeability to gases,[142] and extremely high specific surface area[143]. However, due to the large aspect-ratio, van der Waals interactions, and π-π interactions, exfoliated graphene layers have a strong tendency to aggregate and phase separate, resulting in poorly dispersed bundles and agglomerates in a polymer matrix.[144] Nevertheless, one fundamental property of graphene is that it can be functionalized by oxygen-containing groups such as epoxy, hydroxyl, carbonyl, and carboxylic acid groups. This oxidized form of graphene is known as graphene oxide (GO). The hydrophilicity-hydrophobicity balance of GO, ability to dissolve and form stable colloid solutions in water and a wide range of organic solvents, and better interfacial-bonding capabilities of its functional groups attached to the basal plane and edge, made GO a promising candidate for filler-reinforced polymer composites.

As reported in recent works of literature, the addition of GO in polymer matrices leads to considerable improvements of not only the mechanical properties including strength, toughness, stiffness, and hardness but also the viscoelastic and thermal properties of the virgin polymers.[145-151] Solution blending, melt blending, and in situ polymerization are the three main methods to

prepare GO-based polymer nanocomposites.[152] The homogeneous dispersion and exfoliation of GO sheets in polymer matrices are difficult to achieve in the case of melt blending due to the high viscosities of polymer melts. Besides, GO sheets undergo in situ thermal reduction and lose oxygen-containing functional groups, which leads to a weak interaction between GO sheets and polymer chains, and as a consequence, inferior mechanical properties are observed.[153] Also, melt blending of two immiscible polymers in the presence of nanofillers results in selective localization of nanofillers in only one phase or at the interface of the two phases.[154] This inhomogeneous distribution decreases the reinforcement effect of the nanofillers. Though it is much easier to get uniform dispersion and full exfoliation of GO nanosheets via solution blending, this processing technique is not environmentally friendly, and solvent removal is a critical issue.[155] On the other hand, in situ bulk polymerization is a facile solvent-free method through which graphene can be dispersed homogeneously in polymer matrices.[152]

Copolymerization is an effective way to tune the properties of virgin polymers. For instance, the copolymer of styrene (St) and methyl methacrylate (MMA) combines the excellent ease of processing of polystyrene (PS) with the high-strength and crystal clarity of poly(methyl methacrylate) (PMMA). This copolymer has ubiquitous use in the homeware and toy industries. The monomer ratio and dispersion state of the nanofiller have a strong influence on the polymer nanocomposite properties. Therefore, optimization of the monomer ratios in a copolymer and homogeneous dispersion of the fillers can enhance the mechanical and thermal properties and, in turn, will significantly broaden the scope of the material.

Although organoclay, montmorillonite, graphite, carbon nanotube, and graphene reinforced PS and PMMA immiscible blends prepared by melt mixing or solution blending have been studied before,[153, 154, 156-158] no research article, to date, reported the reinforcement of poly(St-co-MMA)

with GO or even any graphene-related nanomaterials via in situ bulk polymerization and evaluated the effect of GO during and after the copolymerization. Moreover, although poly(St-co-MMA) was synthesized before, to the best of our knowledge, no research has been done to optimize the monomer ratio in terms of mechanical properties. Herein, initially, we optimized the monomer ratio to synthesize poly(St-co-MMA). Later, we tried to improve the mechanical and thermal properties of the material by adding GO at a minimal level. We also performed microstructural and chemical characterizations and analyzed the effect of GO wt.% on the properties of the copolymer. GO is expected to provide better interface bonding and filler loading effect at extraordinarily low filler content predominantly due to functional groups containing many reactive zones. Also, PS is non-polar, whereas PMMA consists of a non-polar hydrocarbon backbone and somewhat polar pendant ester groups. The difference in polarity of the repeating units in the copolymer chain is also anticipated to affect the dispersion morphology of the GO sheets. Furthermore, we devised an ingenious experimental procedure to initiate in-situ copolymerization under ultrasonication at 60 °C to prevent aggregation and achieve high dispersion, a process of prime industrial importance for the preparation of well-dispersed nanocomposites. The prepared strong and thermally stable copolymer nanocomposite should find applications such as in sports, toy, coating, automobile industries, etc.

3.2 Materials and methods

3.2.1 Materials

Styrene (St, 99%) and methyl methacrylate (MMA, 99%) liquid monomers, graphite, hydrogen peroxide (H_2O_2, 30%), sulfuric acid (H_2SO_4, 95.098%), azobisisobutyronitrile (AIBN, 98%) were purchased from Sigma-Aldrich. Potassium permanganate ($KMnO_4$, 99%) was bought from Caledon. Phosphoric acid (H_3PO_4, 85%), methanol, and tetrahydrofuran (THF, 99%) were

purchased from Fisher Scientific. St and MMA liquid monomers were passed through a column packed with Al_2O_3 powder, and AIBN was recrystallized by ethanol. The rest of the chemicals were used as received.

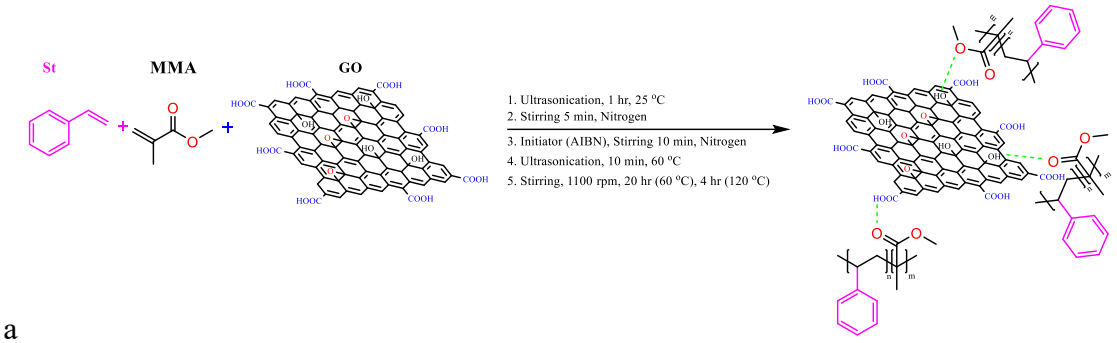

a

b

c

Fig. 3.1 (a) Illustration of the GO reinforced nanocomposites preparation. (b) Cryofractured GO (0.1) sample. (c) Injection-molded dogbones of pure copolymer and nanocomposites**.**

3.2.2 GO synthesis

GO was synthesized following the protocol reported previously.[159] Briefly, a 9:1 mixture of H_2SO_4 (360 ml) and H_3PO_4 (40 ml) was added to 2.5 g of graphite oxide powder under constant magnetic stirring, followed by slow addition of 12.5 g of $KMnO_4$. The reaction was then stirred for 12 h at 50 °C. After overnight oxidation, the color of the mixture turned brown. The reaction was then cooled down to room temperature and slowly poured onto ice-cold water (300 ml) with 30% H_2O_2 (20 ml), which turned the color of the solution to yellow. The bright yellow solution

was kept at room temperature overnight for sedimentation. Later, the transparent upper layer of the solution was removed, and the solid material was washed with water, 30% HCl, and ethanol. To purify GO, the sediments were further washed three times with distilled water using the Buchner funnel. Finally, the filtered solid was freeze-dried overnight to get GO powder.

3.2.3 Copolymer synthesis

To optimize injection moldability and mechanical properties of poly(St-co-MMA), we prepared copolymers containing varying weight percentages of St and MMA monomers. Different ratios of St (10, 30, 50, and 70%) were added to MMA monomer in separate reaction flasks. The mixtures were stirred and purged by nitrogen for 5 min initially. 50 mg of AIBN was then added to each mixture, and the reaction flasks were tightly sealed, followed by stirring and purging with nitrogen for an additional 10 min. The mixtures were ultrasonicated for 10 min at 60 °C to initiate polymerization. The reaction flasks were then submerged in a paraffin oil bath and kept for 20 h at 70 °C, followed by 4 h at 120 °C while stirring at 1100 rpm. After polymerization, the solid copolymers were cryofractured in liquid nitrogen to collect pellets, which were rinsed 3 times with cold methanol for a total of 15 min before drying overnight in a vacuum oven at 80 °C.

3.2.4 Preparation of polymer nanocomposites

GO reinforced copolymer nanocomposites were prepared by in situ bulk polymerization. Typically, St (3.311 ml) and MMA (7.478 ml) using an optimized weight ratio of 30:70 were taken in a reaction flask and stirred at room temperature. GO powder was then added in the reaction flask, and the mixture was ultrasonicated for 1 h to disperse GO homogeneously. Initially, the reaction mixture was stirred and purged with nitrogen for 5 min. AIBN (50 mg) radical initiator was then added to the solution followed by stirring and purging with nitrogen for an additional 10 min and the flask was sealed properly to maintain the nitrogen atmosphere inside the flask. To

initiate polymerization while maintaining high dispersion, the solution was ultrasonicated for 10 min at 60 °C. Later, the reaction flask was submerged in a paraffin oil bath and kept for 20 h at 70 °C, followed by 4 h at 120 °C while stirring at 1100 rpm. After polymerization, the solid nanocomposite was cryofractured in liquid nitrogen to collect pellets, which were rinsed three times with cold methanol for a total of 15 min before drying overnight in a vacuum oven at 80 °C. Nanocomposites containing different GO concentrations (0.075, 0.1, 0.25, 0.5, and 1 wt.%) were prepared following the same procedure. Fig. 3.1a schematically illustrates the preparation process of the nanocomposites. Fig. 3.1b and c shows the actual photographs of the materials.

3.2.5 Injection molding

Standard tensile test ASTM D638 Type V specimens were injection molded using HAAKE MiniJet Pro (Thermo Scientific, Germany). The temperatures of the cylinder and the mold were set at 245 and 70 °C, respectively. Dwell time was set to be 20 sec, and injection pressure was maintained at 300 bar. Notably, the injection molding parameters were optimized for the test, and pellets were used immediately after taking out from the vacuum oven to prevent moisture accumulation.

3.2.6 Mechanical testing

A high-precision Shimadzu Autograph AGS-X instrument equipped with 1000 N static load cell was used to perform tensile tests of the polymer nanocomposites at a cross-head speed of 1 mm/min. Before testing, all the specimens were thoroughly dried in an oven for 4 h at 60 °C to remove any residual gas and moisture contents. At least three specimens were tested for each combination, and the stress-strain curves, ultimate tensile strength, ultimate strain, and Young's modulus of the samples were obtained according to ASTM Standard D638. The viscoelastic response of the neat copolymer and nanocomposites were determined using Dynamic Mechanical

Analysis (DMA Q800, TA Instruments). Strips of uniform width (9.2 mm) and thickness (1.3 mm) were sanded down from injection molded dog bone samples and tested under the nitrogen atmosphere. The amplitude of 20 μm, a static load 0.01N, and a frequency of 1 Hz were applied to the test specimens using a film tension clamp. Storage modulus and tan delta values were obtained as a function of temperature in the range of 30 to 150 °C using the heating ramp of 2 °C min^{-1}. The glass transition temperature (T_g) values were obtained from the tan delta peaks.

3.2.7 Thermal analysis

Differential scanning calorimetry (DSC 2920, TA Instruments) analysis was performed in a controlled nitrogen atmosphere at a heating rate of 5 °C min^{-1}. The thermal stabilities of the specimens were studied using thermogravimetric analysis (TGA Q50, TA Instruments) under a continuous nitrogen flow. Samples were placed in a platinum crucible, and dynamic tests were performed by heating the samples from 25 to 600 °C at a heating ramp of 10 °C min^{-1}. Weight loss was measured as a function of temperature.

3.2.8 Chemical and microstructural characterization

Fourier-transform Infrared Spectroscopy with Attenuated Total Reflectance (FTIR-ATR) measurements was performed on a Bruker Alpha FTIR spectrophotometer. Absorbance spectra were recorded after 64 scans with a resolution of 4 cm^{-1} in the wavenumber range of 4000-410 cm^{-1}. Wide Angle X-ray Diffraction (WAXRD) analyses were performed on a Rigaku Ultima IV fitted with Co-kα (λ = 1.789 Å) source using 38 kV and 38 mA. The samples were scanned from 5° to 50° (2θ) with 0.02 step size and 2° min^{-1} scanning time. The layer spacing was calculated with the aid of Bragg's Law. Weight average molecular weight (M_w) and polydispersity index (PDI) were determined by a gel permeation chromatography (GPC) instrument equipped with a Styragel HR 4E column and 2000 ELSD detector. The samples were dissolved in THF at 0.5 mg mL^{-1}

concentration, and THF was used as eluent with a flow rate of 0.5 ml min^{-1}. Polystyrene standards were used to calibrate the instrument. Bruker Dimension Edge Atomic force microscopy (AFM) with ScanAsyst was used to acquire topographic images. All the photos were taken in tapping mode using silicon cantilever at a scan rate of 10 μm s^{-1} and analyzed using the Nanoscope Analysis software. For imaging, samples were dispersed in THF and cast in aluminum pans. An FEI Morgagni 268 transmission electron microscopy (TEM) instrument, operating at 80 kV, was used to investigate the microstructural morphology of the specimens. The samples were embedded in Spurr's resin and cured at 70 °C. Thin films (80-100 nm thickness) were sectioned using Ultracut E Ultramicrotome and placed on a copper grid (300 mesh) without support film. Scanning electron microscopy (SEM) images were captured using an EVO 10 (Zeiss) at an acceleration voltage of 15 kV. Cryofractured samples were sputter-coated by a thin layer of Au/Pd alloy using an Anatech Hummer Sputtering System before SEM analysis.

3.3 Results and discussion

3.3.1 Characterization of GO

FTIR-ATR spectra of pristine graphite and GO are shown in Fig. 3.2a. The GO exhibits characteristic broad absorption band in the range of ~3000 to 3500 cm^{-1}, which is ascribed to the stretching vibration of O-H groups. The absorption peak observed at 1735 cm^{-1} corresponds to the stretching vibration of C=O bonds in the carboxyl group, while the sharp absorption band at 1614 cm^{-1} is related to the stretching of sp^2 alkene in the unoxidized graphitic domain.[159] The peak at 1221 cm^{-1} can be attributed to C-O vibrations in the carboxylic acid group, and the two broad bands at 1054 and 975 cm^{-1} correspond to the stretching vibrations of the epoxy ring (C-O-C).[160] To understand the atomic structures and interlayer spacing of pristine graphite and GO, WAXRD analysis was carried out, and the results are shown in Fig. 3.2b. The pristine graphite exhibits a

sharp diffraction peak centered at 2θ = 26.4° corresponding to the (0 0 2) graphite plane composed of well-ordered graphenes with a lattice spacing (*d*-spacing) of 0.34 nm. However, GO shows a less intense peak at 2θ = 10.3°, corresponding to a *d*-spacing of 0.83 nm. The relatively larger *d*-spacing of GO than that of pristine graphite is mainly attributed to the presence of oxygen-containing functional groups attached to the edges and the basal planes of GO sheets.[161] Fig. 3.2c is an actual photograph of synthesized GO in a glass vial. TEM image (Fig. 3.2d and e) shows that exfoliation in water and methanol produced individual GO flakes stacked in a laminated structure. Scrolling on the edges and typical wrinkled sheet structures are also identified by TEM, as shown in Fig. 3.2e.

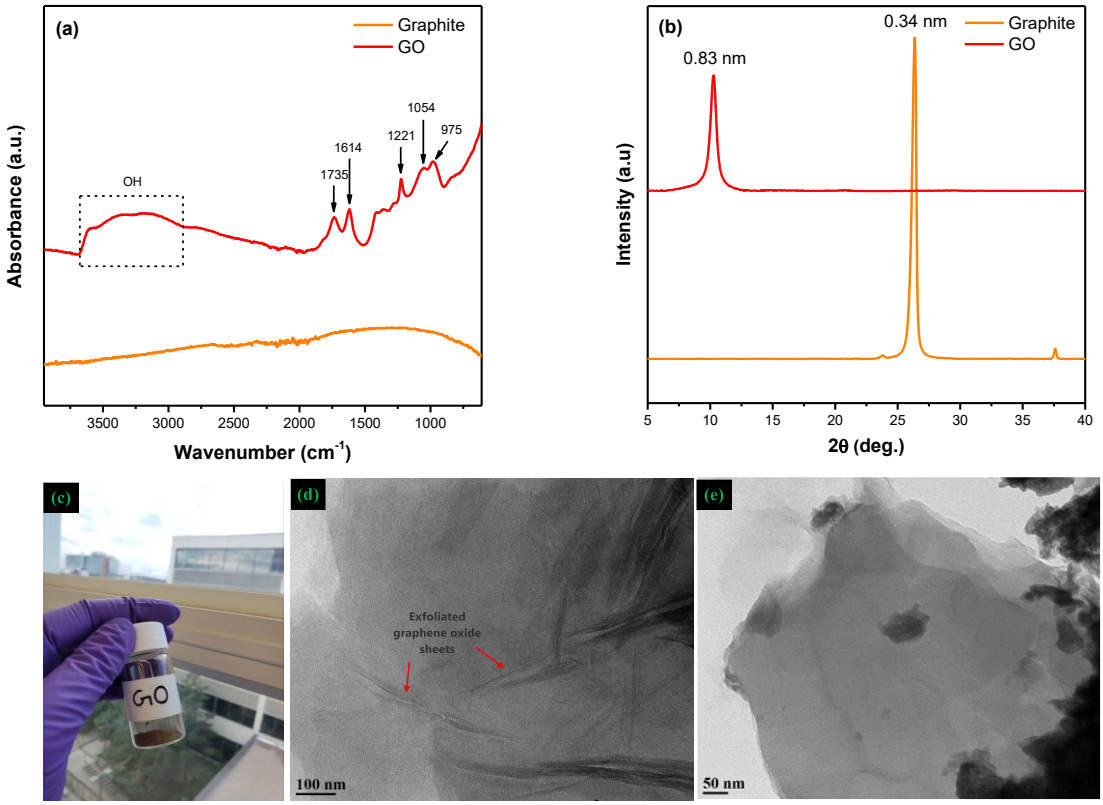

Fig. 3.2 Characterization of GO. (a) FTIR-ATR spectra of pristine graphite and GO. (b) WAXRD spectra of pristine graphite and GO. (c) as-synthesized GO. Typical TEM images of GO sheets in (d) water and (e) methanol solution.

3.3.2 Chemical and crystallographic analysis of nanocomposites

Fig. 3.3a shows FTIR-ATR spectra of neat PS, neat PMMA, neat copolymer with varying ratio of St, and GO (0.1) nanocomposite. PS exhibits several characteristic absorption bands, i.e., C-H stretching vibration at 3100-2840 cm^{-1}, C=C stretching vibration corresponding to the aromatic ring at 1598 and 1500 cm^{-1}, CH_2 bending vibration at 1448 cm^{-1}, C-H in-plane deformation at 1024 cm^{-1}, and C-H out-of-plane bending of the phenyl ring at 754, 691, and 533 cm^{-1}.[162] Meanwhile, the FTIR-ATR spectrum of PMMA shows low-intensity bands in the region 3025-2848 cm^{-1}, which are attributed to symmetric and asymmetric C-H stretching vibrations. A sharp absorption peak originated from the carbonyl (C=O) stretching vibration of the ester group was detected at 1724 cm^{-1}. Also, intensity bands observed at 1480-1355 cm^{-1} and 1270-987 cm^{-1} are ascribed to C-H bending vibration of the $-CH_3$ group and C-O stretching vibrations of the C-O-C moieties, respectively.[163] The spectra of the copolymers show characteristic peaks of both PS and PMMA, and with an increasing fraction of St in the copolymer, the bands related to PS intensified gradually. Interestingly, the spectra of GO (0.1) nanocomposite appear similar to the neat copolymer St(30):MMA(70). This could be due to the overlapping of the absorption peaks related to the functional groups of GO and the neat copolymer. Another rational explanation could be that, GO instituted only intermolecular attraction through, for example, hydrogen bonding, and did not form any strong chemical bond with the copolymer chains.[147] WAXRD analysis has been widely employed for studying the state of dispersion of filler materials in polymer nanocomposites.[164] Herein, the neat copolymer and GO (0.1) nanocomposite were characterized by WAXRD, and their diffraction patterns are presented in Fig. 3.3b.

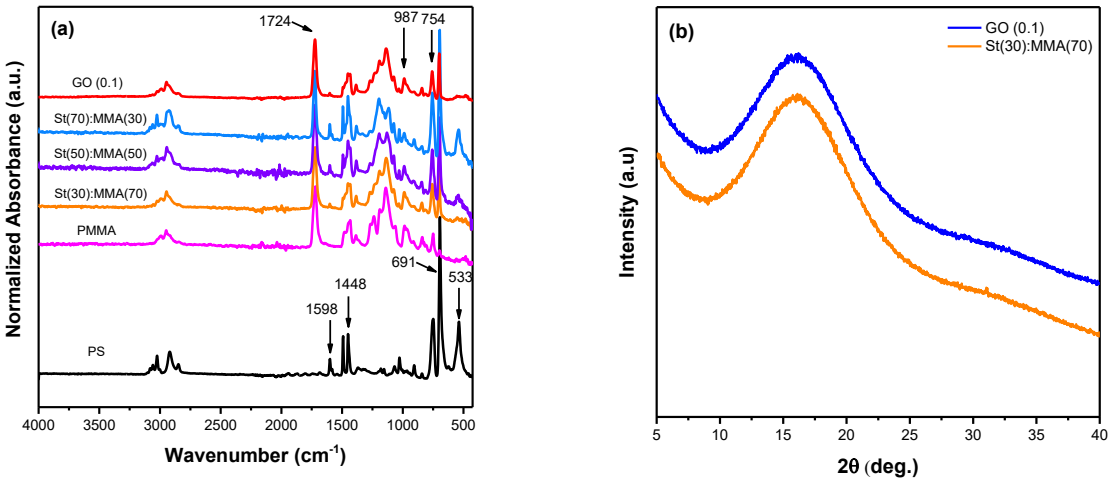

Fig. 3.3 (a) FTIR-ATR spectra and (b) WAXRD profiles of the neat St(30):MMA(70) copolymer and GO (0.1) reinforced nanocomposite.

The WAXRD pattern of the neat sample shows a broad band around 2θ = 16° related to the amorphous structure of the copolymer. Although GO (0.1) nanocomposite exhibits a similar diffraction pattern, it does not show the characteristic peak of GO (2θ = 10.3° as shown in Fig. 3.2b), which indicates that the GO sheets are exfoliated or intercalated in the copolymer matrix. M_w has been found to increase as GO concentration was increased (up to 0.1 wt.%). During copolymerization, especially under ultrasonication at the early stages of initiation, GO might have reduced the efficiency of the initiator by acting as a scavenger, which in turn resulted in a copolymer with a modest increase in molecular weight (Table 3.1).[147] We found, however, a decrease in M_w when GO concentration increased from 0.1 to 1 wt.%.

Table 3.1 M_w and PDI of the neat copolymer and GO reinforced polymer nanocomposites.

Sample	M_w	PDI
Neat copolymer	100,970	1.72
GO (0.075)	111,070	1.84
GO (0.1)	126,270	1.55
GO (0.25)	120,210	1.55
GO (0.5)	98,374	1.58
GO (1)	79,600	1.67

3.3.3 Microstructural characterization

Typical TEM images of the neat copolymer and GO reinforced nanocomposites are illustrated in Fig. 3.4 (a-f). In general, the dark lines and bright areas represent the cross-sections of a single or multiple layers of GO and the copolymer matrix, respectively. Many sparsely dispersed exfoliated, as well as intercalated, GO tactoids were observed in the matrix of GO (0.075) nanocomposite. For GO (0.1), GO sheets were identified; however, some restacking was also observed. In agreement with previous reports,[165, 166] few stacked GO platelets, identified through TEM analysis, did not contribute to the WAXRD signal of GO (0.1) nanocomposite (see Fig. 3.3b), likely because the GO concentration—among which only a fraction of nanosheets formed multilayer stacks—is too low relative to the copolymer. Similarly, homogeneously distributed exfoliated GO sheets were found in both GO (0.25) and GO (0.5) nanocomposites; however, the wrinkled morphology and scrolling of GO sheets along with some aggregated region were visible for only GO (0.5). Meanwhile, poor distribution and severe aggregation of GO sheets were detected in the GO (1) nanocomposite matrix.

GO (0.1) nanocomposite was characterized using AFM in the tapping phase and height sensor modes. Although 3D-topography image (Fig. 3.4h) did not provide any distinction between the GO sheets and copolymer matrix, the comparatively darker regions in the copolymer matrix, detected in the tapping phase mode (Fig. 3.4g), might be attributed to GO sheets distributed in the solvent cast surface of the nanocomposite.[167] Note that ridges and valleys (black and white dots) in the phase image are ascribed to impurities and surface defects. As expected, no phase separation (for example, isolated or continuous island, pitted surface, and granular morphology)[168] of PS and PMMA was observed, which corroborates the successful synthesis of the copolymer; this result is in accordance with TEM analysis of the copolymer as shown in Fig. 3.4a.

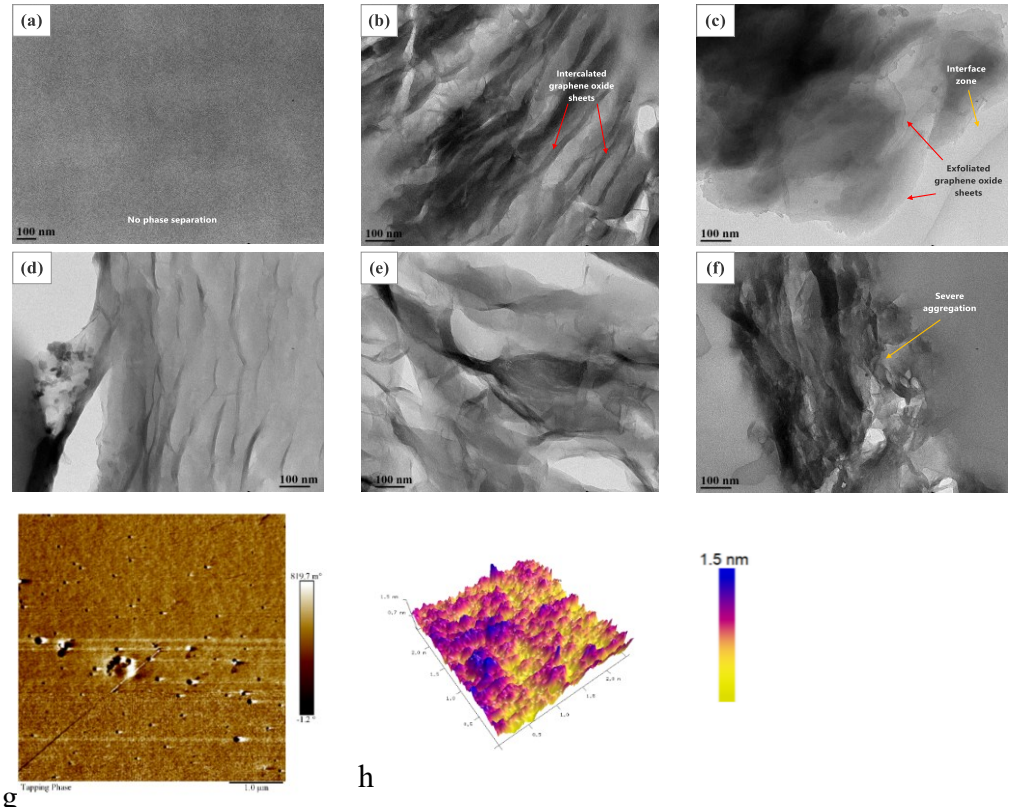

Fig. 3.4 TEM images of the cross-sections of (a) neat copolymer, (b) GO (0.075), (c) GO (0.1), (d) GO (0.25), (e) GO (0.5), and (f) GO (1) nanocomposites. AFM images of the solvent cast surface of GO (0.1) nanocomposite, in (g) tapping phase and (h) height sensor modes.

3.3.4 Tensile testing

First, we optimized the monomer ratios based on mechanical properties. St(10):MMA(90) and St(90):MMA(10) samples exhibited very poor injection moldability and high brittleness thus, we only focused on St(30):MMA(70), St(50):MMA(50), and St(70):MMA(30) samples. The injection molding parameters were optimized accordingly, and dogbone shapes according to ASTM D638 Standard were successfully manufactured. Finally, to get an idea about how the amount of St in the copolymer matrix influences ultimate strength and strain, uniaxial tensile tests were performed (Table 3.2). It was observed that with the increase in St weight fraction, UTS and ultimate strain decrease; however, the elastic modulus was found to increase with the increase in St amount. For further analysis, we have chosen St(30):MMA(70) as it provided the highest UTS.

Table 3.2 Ultimate tensile strength (UTS), ultimate strain, and Young's modulus values of the copolymer and GO reinforced nanocomposites.

Sample	UTS (MPa)	Ultimate strain (%)	Young's modulus (GPa)
St(30):MMA(70)	57.72 ± 5.05	5.58 ± 0.88	2.24 ± 0.10
St(50):MMA(50)	52.42 ± 5.88	3.79 ± 0.89	2.36 ± 0.12
St(70):MMA(30)	49.45 ± 4.36	3.34 ± 0.87	2.64 ± 0.03
GO (0.075)	56.69 ± 3.39	4.78 ± 0.42	2.30 ± 0.37
GO (0.1)	66.14 ± 1.55	6.42 ± 0.32	2.47 ± 0.19
GO (0.25)	64.26 ± 1.97	6.36 ± 0.62	2.56 ± 0.12
GO (0.5)	62.42 ± 3.56	5.20 ± 0.98	2.55 ± 0.22
GO (1)	57.70 ± 2.27	5.25 ± 0.28	2.22 ± 0.19

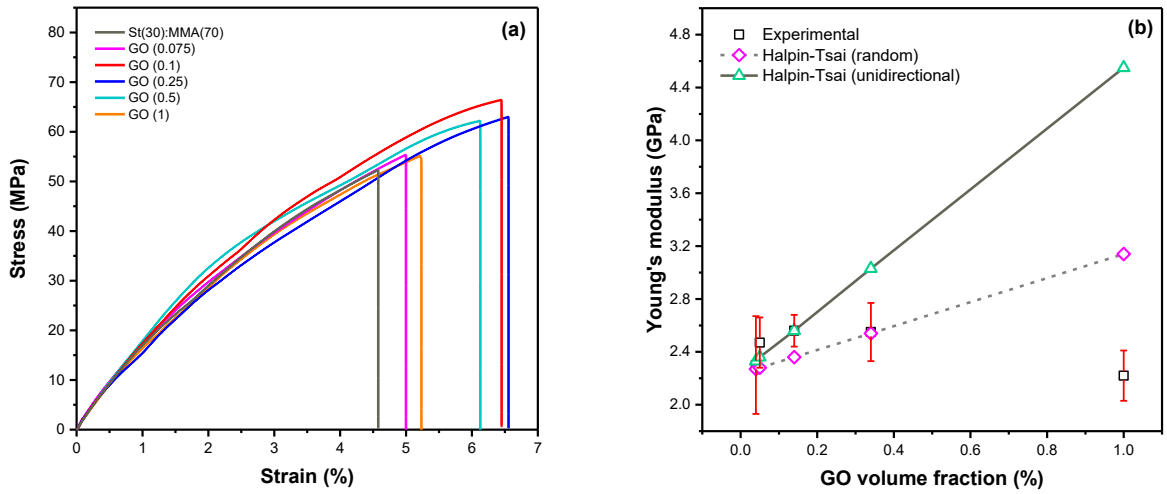

Fig. 3.5 (a) Representative tensile engineering stress-strain curves of the neat copolymer and GO reinforced nanocomposites at room temperature. (b) Comparison of the experimental Young's modulus of GO reinforced nanocomposites to values as calculated from Halpin-Tsai equations.

To provide insight into the strength and ductility of the nanocomposites presented in this work, typical stress-strain curves are plotted in Fig. 3.5a. The curves are almost linear without any significant yielding or cold flow before fracture, which confirms the brittle nature of the materials. Further, tensile tests reveal a noticeable change in tensile strength and strain with the weight fraction of GO. In a typical tensile test, GO (0.1) nanocomposite showed an ultimate tensile strength (UTS) of ~66 MPa (Fig. 3.5a). This strength is 26% higher than the neat copolymer, while the improvement in terms of strain is 40%. Such an outstanding combination between strength and ductility resulted in an 88% increase (from 140.3 to 263.5 Jm^{-3}) in toughness (measures resistance to fracture and can be determined from the area under the stress-strain curve). Functional groups (such as epoxides, alcohols, and carboxylic acids) attached to the basal planes and edges of GO sheets form strong interfacial interaction with groups present on the backbone of copolymer chains through chemical bonding, hydrogen bonding, and π-π stacking.[169] Intrinsic toughening of the

nanocomposites, which is effective against both the initiation and propagation of cracks results, primarily from inelastic deformation or plasticity that is achieved through sliding or slip between GO sheets[170] and micro-cracking mechanisms[152]. However, the principal source of toughness in the nanocomposites is extrinsic, which acts to reduce the local stresses and strains at the crack tip and arises from crack bridging,[171] crack deflection,[172] and crack pinning[150] as growing crack encounters GO sheets. Since cracks always follow the more compliant path, due to elastic modulus mismatch between GO and copolymer matrix, they are drawn to the matrix phase, thus resulting in tortuous and deflected crack paths and pull-out of the GO sheets. It should be noted that the intrinsic and extrinsic mechanisms are coupled, and their synergetic action results in increased resistance to crack initiation and growth of an incipient crack. Joint enhancement of both the strength and toughness—which are mutually exclusive properties—can be beneficial for most engineering structural materials in the aerospace, transportation, or power-generation industries.[78, 173] Meanwhile, average Young's modulus slightly increased from 2.24 to 2.47 GPa (~10% increment) when 0.1 wt.% GO was added to the neat copolymer matrix. The highest Young's modulus (2.56 GPa) is recorded for GO (0.25) (See Table 3.2). Nonetheless, it is also evident from Table 3.2 that UTS increased up to a threshold limit of GO content (0.1 wt.%), then it gradually decreased to ~57 MPa (1 wt.%). The reduction of tensile strength and ultimate strain at higher loadings is attributed to the agglomeration of GO sheets due to poor dispersion into the copolymer matrix. On average, although GO (0.075) nanocomposite has better stiffness (2.30 GPa), the ultimate strength and strain are marginally lower than that of the pure copolymer. It is known that the tensile properties of the injection-molded samples are subjected to filler alignment and orientation through the shear-induced flow. Perhaps, the observed result for GO (0.075) is dominated by such extrinsic factors accompanied by structural defects of GO sheets such as atomic

vacancies, topological defects. Moreover, the GO content could be too low to provide any reinforcing effect. Another point to be noted is that, for injection molding, often higher cylinder/injection temperature (above 200 °C) is used for PS or PMMA related polymers, however, GO loses some labile oxygenated functional groups around this temperature (see Fig. 3.9), which may reduce reinforcing effect.

The Halpin-Tsai model, a widely used model to predict Young's modulus of unidirectional or randomly distributed filler-reinforced nanocomposites,[174, 175] was used in this study to simulate modulus of the GO reinforced nanocomposites. The Young's modulus of the unidirectional (E_c) and randomly oriented ($E_{||}$) GO-reinforced nanocomposites are given by

$$E_c = E_m \left[\frac{3}{8}\frac{1+\eta_L \xi V_c}{1-\eta_L V_c} + \frac{5}{8}\frac{1+2\eta_T V_c}{1-\eta_T V_c}\right] \tag{3.1}$$

$$E_{||} = E_m \left[\frac{1+\eta_L \xi V_c}{1-\eta_L V_c}\right] \tag{3.2}$$

$$\eta_L = \frac{\left(\frac{E_g}{E_m}\right) - 1}{\left(\frac{E_g}{E_m}\right) + \xi} \tag{3.3}$$

$$\eta_T = \frac{\left(\frac{E_g}{E_m}\right) - 1}{\left(\frac{E_g}{E_m}\right) + 2} \tag{3.4}$$

$$\xi = \frac{2\alpha_g}{3} = \frac{2l_g}{3t_g} \tag{3.5}$$

Where E_g and E_m represent Young's modulus of the GO (0.25 TPa)[176] and the copolymer matrix (2.24 GPa, from the experimental data). α_g, l_g, and t_g stand for the aspect ratio, length (2.5 μm),[174] and thickness (1.1 nm)[159] of the GO sheet. The volume fraction of GO in the nanocomposites is

represented by V_c. Herein, the weight fraction of GO is converted to volume fraction by using the following equation

$$v = \frac{w\rho_M}{w\rho_M + (1-w)\rho_g} \tag{3.6}$$

Where v and w refer to the volume fraction and weight fraction of GO. The density of the copolymer (ρ_M) and GO (ρ_g) are 1.14 g cm^{-3} and 2.2 g cm^{-3},[174] respectively. 0.04, 0.05, 0.14, 0.34, and 1 volume fractions, corresponding to the weight fraction values used in our experiment, were utilized to calculate the modulus of the nanocomposites. Substituting these parameters into Eqns. 3.1 – 3.5, Young's modulus of the nanocomposites was calculated considering the following assumptions: (i) GO sheet and matrix are linearly elastic, isotropic, and firmly bonded, (ii) GO is asymmetric and uniform in size and shape, (iii) Young's modulus of the GO and matrix are considered to be identical to those of the pure components, (iv) platelets are fully exfoliated. As shown in Fig 3.5b, good agreement was found between the experimental data and the theoretical simulation results obtained from the Halpin-Tsai (unidirectional) model, especially at low filler loadings (<0.14 vol.% or <0.25 wt.%), which suggests that GO sheets are aligned parallel to the surface of the nanocomposite films. However, in the case of 0.34 vol.% of GO, experimental modulus matches with predicted value from the Halpin-Tsai (random) model. As expected, the experimental value differs largely with the theoretical value of Young's modulus of GO (1) nanocomposite. This is mainly due to the agglomeration of GO sheets, which has not been considered in theoretical modeling.

To identify traces of intrinsic and extrinsic toughening mechanisms, microscopic features of the cryofractured surfaces are studied using SEM (Fig. 3.6). Evidence of both types of toughening mechanisms are present on the fractured surfaces of the nanocomposites (Fig. 3.6b-f); however, the mirror-like fracture surface of the neat copolymer, as shown in Fig. 3.6a, reveals its nature of

weak resistance to crack initiation and propagation. Tortuous crack paths, crack deflection, and river patterns with several protruding GO sheets on the nanocomposites suggest strong interfacial adhesion between the functional groups of GO and copolymer chains.[177, 178] The restacking and aggregation of GO sheets are visible in Fig. 3.6f that indicates non-uniform dispersion and weak interaction between the filler and copolymer matrix phase at higher loadings, which is consistent with TEM analysis (see Fig. 3.4).

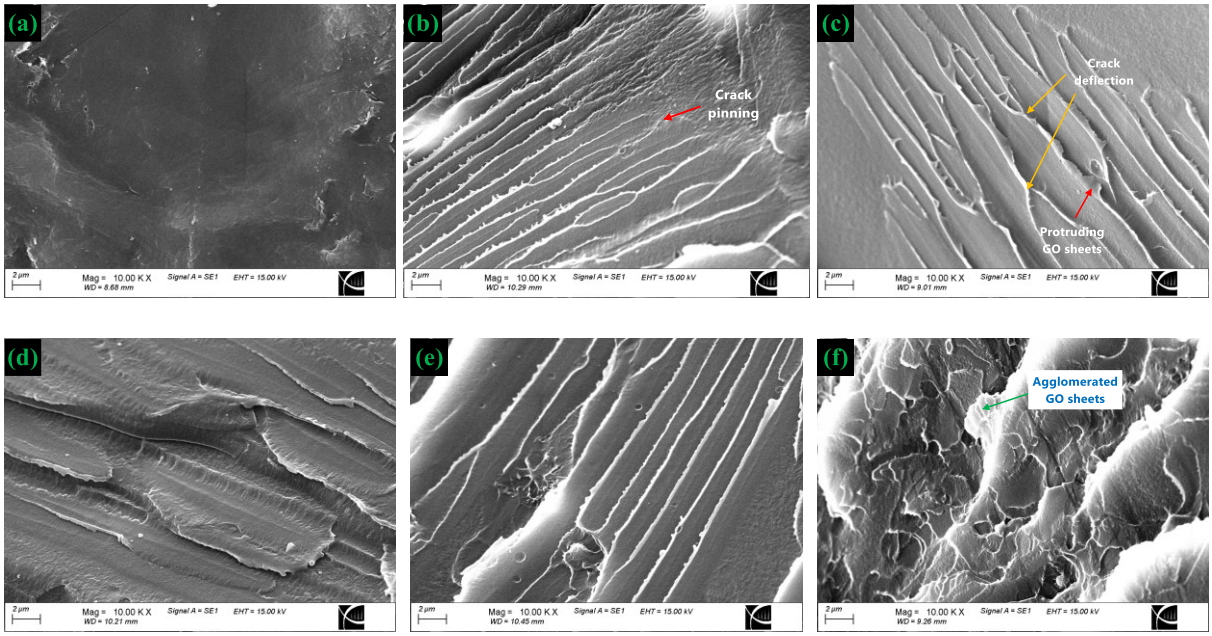

Fig. 3.6 SEM images of the cryofractured surfaces of (a) the neat copolymer, (b) 0.075, (c) 0.1, (d) 0.25, (e) 0.5, and (f) 1 wt.% GO reinforced nanocomposites.

3.3.5 Thermomechanical analysis

The remarkable enhancement in storage modulus, the ability of the material to store energy, is achieved by incorporating GO in the copolymer matrix (Fig. 3.7), especially in the glassy state. The largest increase in storage modulus, at 35 °C, was recorded for GO (0.1) nanocomposite, which is about 43%. GO reinforced nanocomposites also demonstrated an increase in storage modulus in the glass transition region. As an example, the storage modulus of GO (0.25) at 100

°C is 2124 MPa, which is ~37% higher than the neat copolymer. On the other hand, the storage modulus of GO (0.1) drops to 1910 MPa from 3507 MPa at 100 °C; nonetheless, this modulus value is still ~24% higher than the pure sample. In the transition region, polymer chains gain sufficient thermal energy to overcome the barrier for rotational or translational motion and begin sliding past one another at a noticeable rate; thus, the material loses its stiffness. GO sheets, distributed homogeneously in the matrix phase, impede this segmental mobility due to mechanical interlocking, and provide an enhancement in storage modulus in both the glassy and rubbery regions.[179, 180] Note that no apparent difference in storage moduli was observed in the rubbery plateau region, i.e., a temperature higher than 120 °C. As expected, the storage modulus is also highly influenced by the dispersion state of GO in the copolymer matrix. The significant drop in modulus at higher GO loadings, as shown in Fig. 3.7a is mainly due to the aggregation of GO sheets (consistent with UTS results from tensile testing). Fig. 3.7b shows damping or loss factor (tan δ) curves of the injection-molded neat sample and GO reinforced nanocomposites as a function of temperature. The peak of the tan δ curve is often used to determine the T_g of a material. Interestingly, the addition of GO in the copolymer matrix did not yield any considerable changes in T_g (see Table 3.3).

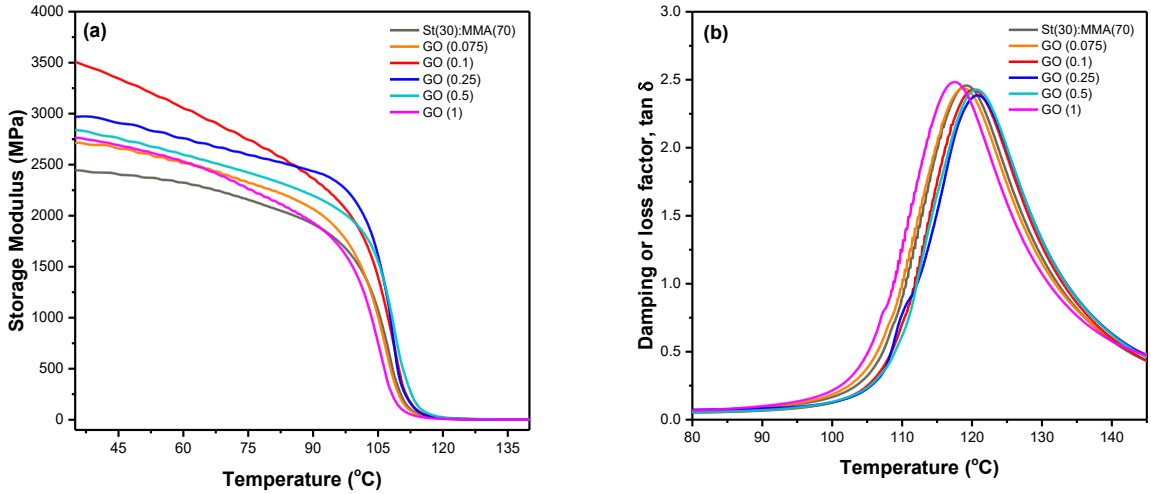

Fig. 3.7 (a) Storage modulus and (b) damping or loss factor (tan δ) of the neat copolymer and GO reinforced nanocomposites as a function of temperature.

3.3.6 Thermal transitions

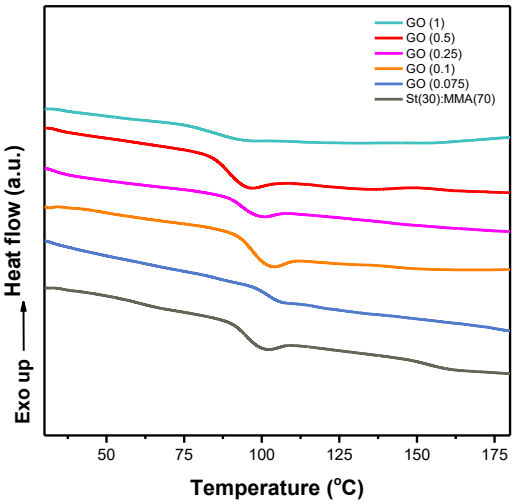

Fig. 3.8 DSC thermographs of the neat copolymer as well as GO reinforced nanocomposites.

The thermal transitions of the as-synthesized materials were examined by DSC (Fig. 3.8). Broad endothermic peaks related to T_g are visible for the neat copolymer and nanocomposites. In comparison to PMMA (105 °C), St(30):MMA(70) has a slightly lower T_g (95.1 °C), which is per the value reported in the literature.[162] No crystallization and melting peaks were observed for the

samples, which might be due to the amorphous nature of both PS and PMMA. The addition of a very low amount of GO (0.075 wt.%) increased the T_g by ~7 °C—this is in contrast to our findings from tan δ plots of injection molded samples (Fig. 3.7b). This difference is likely due to the chain rearrangement or changes in filler distribution caused by injection molding. Nonetheless, the rise in T_g upon inclusion of GO can be attributed to the reduction of chain mobility in the vicinity of GO surfaces, resulting from the strong interaction between the GO sheets and copolymer chains.[149, 175] Further, the dispersion state of the GO sheets significantly influences the intensity of the interaction, in consequence, polymer chain dynamics. As shown in Fig. 3.8 and Table 3.3, T_g decreased to 86 °C from 102 °C with increasing GO concentration since, GO sheets tend to agglomerate more frequently at higher loadings, which eventually leads to ineffective restriction of chain mobility. Another possible reason is the increase in free volume and the loosened molecular packing of the chains

Table 3.3 T_g of the neat copolymer and GO reinforced nanocomposites measured by DSC and DMA techniques.

Sample	T_g (°C), DSC	T_g (°C), DMA
St(30):MMA(70)	95.1	119.2
GO (0.075)	102.2	118.7
GO (0.1)	96.9	120.2
GO (0.25)	93.5	120.7
GO (0.5)	89.4	120.6
GO (1)	86.1	117.5

3.3.7 Thermal stability

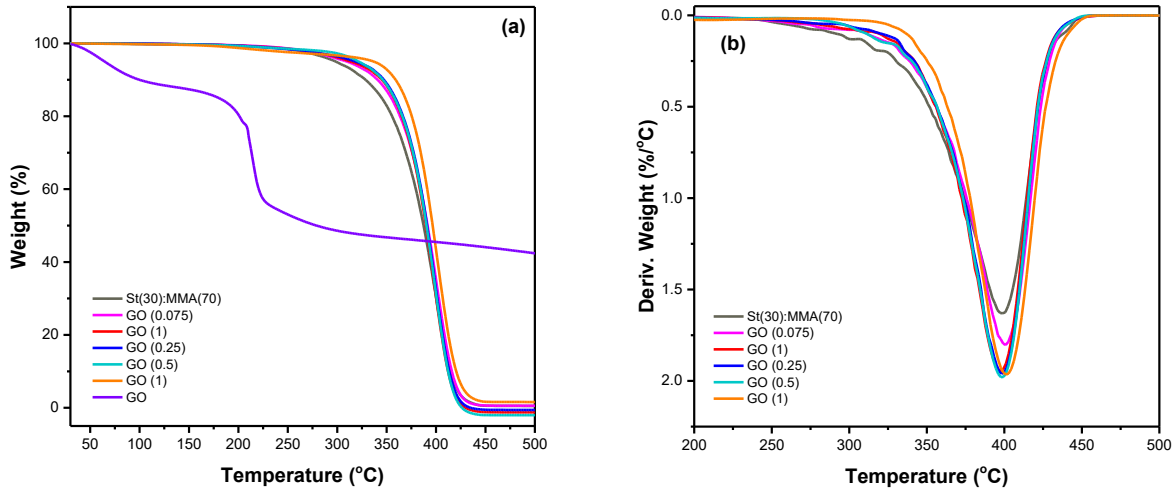

Fig. 3.9 (a) TGA curves of the neat copolymer, GO, and GO reinforced nanocomposites. (b) DTG curves of the neat copolymer and GO reinforced nanocomposites.

To evaluate non-oxidative thermal stability and thermal degradation behaviors, TGA curves, and the first derivatives of the TGA curves (derivative thermogravimetry, DTG) of the materials are plotted in Fig. 3.9. Two distinct mass-loss stages were observed in the case of GO. The first stage (around ~100 °C) is primarily attributed to the evaporation of absorbed water, while the second stage (between ~200 to 220 °C), where GO losses a significant amount of mass (~40%), is caused by the decomposition of labile oxygenated functional groups.[181] On the other hand, the steady weight loss, in the temperature range of 220 to 500 °C, is due to the pyrolysis of residual char. However, the weight loss profiles of the neat copolymer and nanocomposites reveal a single-stage degradation. This primary degradation stage is ascribed to the depolymerization, decomposition, and random scission of the copolymer chains.[147] The lack of additional degradation stages at lower temperature range indicates that there is little or no unreacted monomers or oligomers (see Fig. 3.9a). The differences in degradation profiles can be visualized easily through DTG plots (Fig. 3.9b). Herein, the respective temperatures of 10% (T_{10}), 50% (T_{50}), and 90% (T_{90}) weight losses

were chosen to compare the thermal stability of different samples (Table 3.4). The result strongly implies that the addition of GO improves the thermal stability of the copolymer. Adding 1 wt.% GO, for instance, enhanced T_{10}, T_{50}, and T_{90} by 30, 9, and 5 °C, respectively, as compared to the neat copolymer. Even as little as 0.075 and 0.1 wt.% of GO addition increased T_{10} by 12 and 17 °C, respectively. The thermal degradation of the nanocomposites was delayed mostly due to the excellent thermal stability of GO sheets. In particular, the high aspect-ratio GO sheets acted as a physical barrier to recede emission of thermally decomposed products from the copolymer matrix; hence, they improved the overall thermal stability.[47]

Table 3.4 Thermal degradation temperatures for 10, 50, and 90% weight loss of the neat copolymer and GO reinforced nanocomposites measured by TGA.

Sample	$T_{10\%}$ (°C)	$T_{50\%}$ (°C)	$T_{90\%}$ (°C)
St(30):MMA(70)	327	387	414
GO (0.075)	339	390	416
GO (0.1)	344	389	412
GO (0.25)	345	390	413
GO (0.5)	345	390	413
GO (1)	357	396	419

3.4 Conclusion

In this article, we optimized the monomer ratio of styrene and methyl methacrylate to synthesize poly(styrene-co-methyl methacrylate) copolymer, and reported the effect of GO on the microstructural, mechanical, and thermal behavior of the optimized copolymer, and further

elucidated the reinforcement effect by varying GO content from 0.075 to 1 wt.%. The injection-molded GO (0.1) nanocomposite exhibited a ~14.6% improvement in strength and a ~15% increase in ductility, leading to a notable enhancement of toughness. Both intrinsic and extrinsic toughening mechanisms were discussed, and evidence of crack deflection, pull-out, and restacking of GO-sheets were detected through SEM analysis of the cryofractured surfaces. Furthermore, ~43% improvement of storage modulus was achieved by the addition of only 0.1 wt.% GO. TEM and WAXRD analysis revealed exfoliated morphology of GO-sheets in the matrix of GO (0.1) nanocomposite, however, severe aggregation was observed when the copolymer was reinforced with 0.5 and 1 wt.% GO, as evidenced by TEM and SEM observations. Although the injection-molded samples did not yield any considerable changes in T_g, the as-synthesized samples before injection molding provided up to a ~7 °C increase in T_g. GO-reinforced nanocomposites also exhibited better thermal stability as compared to the pure copolymer. Considering the facile preparation method, a variety of future GO-reinforced copolymer nanocomposites can be prepared by taking advantage of potential reaction sites of GO and balance between hydrophilicity-hydrophobicity. Finally, it can be envisioned that the GO-reinforced copolymers might have major potential applications in sports, multi-functional coatings, housewares, toys, and automobile industries.

3.5 Acknowledgment

The authors acknowledge the partial financial support from the Natural Sciences and Engineering Research Council of Canada (NSERC) and Alberta Innovates.

4. Conclusions and future work

4.1 Combined summary

Plastic production and afterlife of plastic goods are the major sources of environmental and marine pollution. Oil and natural gas are the primary raw-materials for almost 90% of the commercially available plastic products. The extraction of oil and natural gas and the chemical processes to convert them into monomers release a large amount of CO_2-equivalent emissions into the atmosphere. One way to reduce the emission is to partially or fully replace fossil-fuel-based raw-materials with biomass. On the other hand, a large portion of plastic products is thrown away as trash into the landfills after their usual service-life, which ultimately travel to the oceans and beaches, and causes the death of thousands of marine animals each and every year. The thermosets and elastomers occupy half of the total plastic market. Since none of these commercially available polymers is reprocessable nor biodegradable as a result, they are the main contributor to the plastic waste generation and marine pollution. Therefore, the development and production of cross-linked reprocessable thermosets and elastomers can substantially reduce the plastic pollution. Besides, self-healability feature of the polymeric materials can provide increased service-life and reliability of the plastic goods, which, in turn, can reduce the total plastic waste generation per year. However, it is very difficult to synthesize polymeric materials that allow self-healability. Also, most of the self-healable polymeric materials reported in the literature are synthesized from fossil-fuel based resources. Though these materials aid to increase service-life and reduce the cost associated with inspection, they contribute to GHG emissions to an extent. Another way to increase service-life and durability of plastics is through the development of polymer nanocomposites, having better

mechanical and thermal properties as compared to the virgin polymers. The fabrication of polymer nanocomposites is also challenging as the homogeneous dispersion and distribution of the filler materials in a polymer matrix require careful chemical design and research. Though the dispersion morphology of the nanomaterials (e.g., graphene, GO, etc.) in homogeneous polymeric matrices has been studied extensively in the last decade, dispersion morphology in the copolymer matrices has not been given much attention. This thesis addressed the environmental related issues and contributes by providing plausible strategies to mitigate plastic pollution and to increase durability of polymeric materials.

The strategy proposed in **Chapter 2** has the potential to provide an eco-friendly solution to address the environmental challenges associated with the extraction of raw materials from petroleum-based resources, and severe landfill and marine pollution caused by polymeric materials. A novel partially bio (canola oil) based elastomer is reported herein, which not only has the ability of self-healing but also fully recyclable and 3D printable. The electron-deficient terminal C=C bonds of the diacrylate monomer were chemically cross-linked with a thiol-groups containing silicon-based copolymer via a combination of photo-mediated free-radical thiol-ene addition and nucleophile-mediated thiol-Michael addition, both of which are considered as click chemistry reactions. It was found that the silicon-based copolymer can readily be oxidized using a highly efficient hypervalent iodine (III) oxidant to introduce disulfide bonds in the copolymer matrix, and the concentration of the disulfide bonds can be controlled by varying the oxidant concentration. These disulfide bonds can undergo dynamic disulfide metathesis reaction with the aid of a phosphine salt catalyst to facilitate the intrinsic self-healing mechanism. Besides, a successful attempt was made to develop a photocurable ink based on these substances to use in an inkjet 3D printing system. Through gel content measurement and cross-linking density calculation,

it was verified that the 3D printed elastomer has a high degree of cross-linking. The chemical structure of the elastomer and monomers were characterized by FTIR-ATR and XPS. The rheology of the ink was also studied, which revealed that the ink acts as a shear-thinning fluid. Self-healing and reprocessability were demonstrated by conducting uniaxial tensile tests of the healed and reprocessed samples. The tensile strength and strain of the elastomer were found to be 51.9 ± 0.1 kPa and 24.2 ± 0.28%. Remarkably, the healed and reprocessed samples showed mechanical properties and thermal stabilities comparable to the original, with self-healing and reprocessing efficiencies of ~86 and ~124%, respectively. Moreover, the elastomer showed excellent thermal stability before and also after reprocessing; 5% and 50% weight loss temperatures were found to be ~348 and ~504 °C. The service-temperature window of the elastomer was also found to be considerably large, as T_g of the material is -115 °C. The 3D printed elastomer should find applications in soft-robotics, wearable flexible-electronics, and biomedical devices. Furthermore, this work will inspire the development of novel 3D printable fully or partially bio-based elastomers that have both the self-healing and recycling attributes.

Chapter 3 provides a methodology for uniform dispersion of GO in copolymer matrices to attain high toughness and thermal stability. The optimization of monomer ratios of the poly(styrene-*co*-methyl methacrylate), and a facile method to fabricate graphene oxide (GO) reinforced nanocomposites using an in situ bulk copolymerization are reported. The ultimate tensile strength, failure strain, and storage modulus of the copolymer were increased by 14.6, 15, and 43%, respectively, by adding only 0.1 wt.% GO. The copolymer nanocomposites also exhibited better thermal stability compared to the neat sample. Crack arresting mechanisms and dispersion state of GO sheets in the copolymer matrices were investigated using WAXRD, SEM, and TEM. Additionally, the reinforced nanocomposite displayed a ~7 °C higher T_g than the neat copolymer.

Finally, it can be envisioned that the GO-reinforced copolymer might have potential applications in sports equipment, multi-functional coatings, housewares, toys, and automobile industries.

4.2 Future directions

It is noteworthy that the elastomer reported in **Chapter 2** has relatively high elasticity and low strength, which can be improved by incorporating a cyclic compound (ring compound) in AEOD or through epoxidation of the unsaturated bond. Another strategy would be to use a different thiol-containing monomer with a rigid structure. The best approach to increase the mechanical properties is by reinforcing the elastomer with functional nanomaterials. For example, cellulose nanocrystals can be functionalized with an alkene or acrylate to introduce terminal C=C bonds. These bonds will also react with the free thiols during UV-curing and will provide not only physical but also strong chemical interaction between the nanomaterial and the matrix phase. In the future, attempts can be made to synthesis a fully bio-elastomer. For instance, thiol-containing monomer can be synthesized by reacting limonene with thioaceticacid, followed by transesterification with methanol. These types of bio-based monomers, instead of MMDS, can be partially oxidized and cross-link with AEOD. Finally, the design of experiments can be carried out to optimize DLP 3D printing parameters to print 3D objects successfully.

Also note that, the standard deviation of the tensile strength of the self-healed elastomer reported in **Chapter 2** is very high. This is because two specimens among the three broke at the self-healed region, as a result slightly lower tensile strengths were recorded for those specimen. On the other hand, one specimen did not break at the self-healed region thus, for that specimen high tensile strength was recorded. Due to limitation of the material, we could not perform more replications. In future, more replications of the healed samples should be performed to attain Six Sigma Quality.

For **Chapter 3**, functionalized-GO could be used to achieve better matrix-filler interaction effects. Trial experiments were conducted using different concentrations of thermally reduced GO; however, proper dispersion and exfoliation of the reduced GO were not achieved. As a result, no improvement in mechanical properties was observed. More work is needed to improve the dispersion status by attaching other molecules to the functional groups of GO. 3D printability of the material can also be tested in future works.

5. Bibliography

1. Europe, P., Plastics—The Facts 2016. *An analysis of European plastics production, demand and waste data* **2016**, 1-38.

2. Geyer, R.; Jambeck, J. R.; Law, K. L., Production, use, and fate of all plastics ever made. *Science advances* **2017,** 3, (7), e1700782.

3. Kaplan, S., By 2050, there will be more plastic than fish in the world's oceans, study says. *The Washington Post* **2016,** 20.

4. Roser, H. R. M. Plastic Pollution. https://ourworldindata.org/plastic-pollution

5. Zheng, J.; Suh, S., Strategies to reduce the global carbon footprint of plastics. *Nature Climate Change* **2019,** 9, (5), 374-378.

6. Chen, G.-Q.; Patel, M. K., Plastics derived from biological sources: present and future: a technical and environmental review. *Chemical reviews* **2012,** 112, (4), 2082-2099.

7. Spierling, S.; Knüpffer, E.; Behnsen, H.; Mudersbach, M.; Krieg, H.; Springer, S.; Albrecht, S.; Herrmann, C.; Endres, H.-J., Bio-based plastics-a review of environmental, social and economic impact assessments. *Journal of Cleaner Production* **2018,** 185, 476-491.

8. Gandini, A.; Lacerda, T. M.; Carvalho, A. J.; Trovatti, E., Progress of polymers from renewable resources: furans, vegetable oils, and polysaccharides. *Chemical reviews* **2016,** 116, (3), 1637-1669.

9. Dietrich, K.; Bonatz, E.; Geistlinger, H.; Herma, H.; Nastke, R.; Purz, H. J.; Schlawne, M.; Teige, W., Amino resin microcapsules. II. Preparation and morphology. *Acta polymerica* **1989,** 40, (5), 325-331.

10. Hillewaere, X. K.; Du Prez, F. E., Fifteen chemistries for autonomous external self-healing polymers and composites. *Progress in Polymer Science* **2015,** 49, 121-153.

11. Li, X.; Yu, R.; He, Y.; Zhang, Y.; Yang, X.; Zhao, X.; Huang, W., Self-healing polyurethane elastomers based on a disulfide bond by digital light processing 3D printing. *ACS Macro Letters* **2019,** 8, (11), 1511-1516.

12. Canadell, J.; Goossens, H.; Klumperman, B., Self-healing materials based on disulfide links. *Macromolecules* **2011,** 44, (8), 2536-2541.

13. Lei, Z. Q.; Xiang, H. P.; Yuan, Y. J.; Rong, M. Z.; Zhang, M. Q., Room-temperature self-healable and remoldable cross-linked polymer based on the dynamic exchange of disulfide bonds. *Chemistry of Materials* **2014,** 26, (6), 2038-2046.

14. Yu, K.; Xin, A.; Du, H.; Li, Y.; Wang, Q., Additive manufacturing of self-healing elastomers. *NPG Asia Materials* **2019,** 11, (1), 1-11.

15. Liu, Z.; Hong, P.; Huang, Z.; Zhang, T.; Xu, R.; Chen, L.; Xiang, H.; Liu, X., Self-healing, reprocessing and 3D printing of transparent and hydrolysis-resistant silicone elastomers. *Chemical Engineering Journal* **2020,** 387, 124142.

16. Wallin, T.; Pikul, J.; Bodkhe, S.; Peele, B.; Mac Murray, B.; Therriault, D.; McEnerney, B.; Dillon, R.; Giannelis, E.; Shepherd, R., Click chemistry stereolithography for soft robots that self-heal. *Journal of Materials Chemistry B* **2017,** 5, (31), 6249-6255.

17. Acosta Ortiz, R.; Acosta Berlanga, O.; García Valdez, A. E.; Aguirre Flores, R.; Télles Padilla, J. G.; Méndez Padilla, M. G., Self-healing photocurable epoxy/thiol-ene systems using an aromatic epoxy resin. *Advances in Materials Science and Engineering* **2016,** 2016.

18. Xiang, H.; Yin, J.; Lin, G.; Liu, X.; Rong, M.; Zhang, M., Photo-crosslinkable, self-healable and reprocessable rubbers. *Chemical Engineering Journal* **2019,** 358, 878-890.

19. Terryn, S.; Brancart, J.; Lefeber, D.; Van Assche, G.; Vanderborght, B., Self-healing soft pneumatic robots. *Science Robotics* **2017,** 2, (9).

20. Oh, J. Y.; Son, D.; Katsumata, T.; Lee, Y.; Kim, Y.; Lopez, J.; Wu, H.-C.; Kang, J.; Park, J.; Gu, X., Stretchable self-healable semiconducting polymer film for active-matrix strain-sensing array. *Science advances* **2019,** 5, (11), eaav3097.

21. Tan, Y. J.; Godaba, H.; Chen, G.; Tan, S. T. M.; Wan, G.; Li, G.; Lee, P. M.; Cai, Y.; Li, S.; Shepherd, R. F., A transparent, self-healing and high-κ dielectric for low-field-emission stretchable optoelectronics. *Nature Materials* **2020,** 19, (2), 182-188.

22. Ge, G.; Lu, Y.; Qu, X.; Zhao, W.; Ren, Y.; Wang, W.; Wang, Q.; Huang, W.; Dong, X., Muscle-Inspired Self-Healing Hydrogels for Strain and Temperature Sensor. *ACS nano* **2019,** 14, (1), 218-228.

23. Li, J.; Geng, L.; Wang, G.; Chu, H.; Wei, H., Self-healable gels for use in wearable devices. *Chemistry of Materials* **2017,** 29, (21), 8932-8952.

24. Wirthl, D.; Pichler, R.; Drack, M.; Kettlguber, G.; Moser, R.; Gerstmayr, R.; Hartmann, F.; Bradt, E.; Kaltseis, R.; Siket, C. M., Instant tough bonding of hydrogels for soft machines and electronics. *Science advances* **2017,** 3, (6), e1700053.

25. Tallia, F.; Russo, L.; Li, S.; Orrin, A. L.; Shi, X.; Chen, S.; Steele, J. A.; Meille, S.; Chevalier, J.; Lee, P. D., Bouncing and 3D printable hybrids with self-healing properties. *Materials Horizons* **2018,** 5, (5), 849-860.

26. Wang, Z.; An, G.; Zhu, Y.; Liu, X.; Chen, Y.; Wu, H.; Wang, Y.; Shi, X.; Mao, C., 3D-printable self-healing and mechanically reinforced hydrogels with host–guest non-covalent interactions integrated into covalently linked networks. *Materials Horizons* **2019,** 6, (4), 733-742.

27. Gordon, K. L.; Siochi, E. J., Mechanoresponsive healing polymers. In Google Patents: 2018.

28. Gordon, K. L.; Zavada, S. R.; Scott, T. F., Multi-Layered Self-Healing Material System Towards Impact Mitigation. In Google Patents: 2016.

29. Parrish, C. F., Process for self-repair of insulation material. In Google Patents: 2007.

30. Jolley, S. T.; Williams, M. K.; Gibson, T. L.; Smith, T. M.; Caraccio, A. J.; Li, W., Self-healing polymer materials for wire insulation, polyimides, flat surfaces, and inflatable structures. In Google Patents: 2019.

31. Gibson, I.; Rosen, D. W.; Stucker, B., *Additive manufacturing technologies*. Springer: 2014; Vol. 17.

32. Jacobs, P. F., *Rapid prototyping & manufacturing: fundamentals of stereolithography*. Society of Manufacturing Engineers: 1992.

33. Sheoran, A. J.; Kumar, H., Fused Deposition modeling process parameters optimization and effect on mechanical properties and part quality: Review and reflection on present research. *Materials Today: Proceedings* **2020,** 21, 1659-1672.

34. Riggs, B. C.; Elupula, R.; Grayson, S. M.; Chrisey, D. B., Photonic curing of aromatic thiol–ene click dielectric capacitors via inkjet printing. *Journal of Materials Chemistry A* **2014,** 2, (41), 17380-17386.

35. Fong, J.; Xu, P., Thiol-ene inks for 3D printing. In Google Patents: 2019.

36. Li, L.; Lin, Q.; Tang, M.; Duncan, A. J.; Ke, C., Advanced Polymer Designs for Direct-Ink-Write 3D Printing. *Chemistry–A European Journal* **2019,** 25, (46), 10768-10781.

37. González-Henríquez, C. M.; Sarabia-Vallejos, M. A.; Rodriguez-Hernandez, J., Polymers for additive manufacturing and 4D-printing: Materials, methodologies, and biomedical applications. *Progress in Polymer Science* **2019,** 94, 57-116.

38. Truby, R. L.; Lewis, J. A., Printing soft matter in three dimensions. *Nature* **2016,** 540, (7633), 371-378.

39. Aguilera, A. F. E.; Nagarajan, B.; Fleck, B. A.; Qureshi, A. J., Ferromagnetic particle structuring in material jetting-Manufacturing control system and software development. *Procedia Manufacturing* **2019,** 34, 545-551.

40. Koo, J. H., *Polymer nanocomposites*. McGraw-Hill Professional Pub.: 2006.

41. Tjong, S. C., Structural and mechanical properties of polymer nanocomposites. *Materials Science and Engineering: R: Reports* **2006,** 53, (3-4), 73-197.

42. Crosby, A. J.; Lee, J. Y., Polymer nanocomposites: the “nano” effect on mechanical properties. *Polymer reviews* **2007,** 47, (2), 217-229.

43. Han, Z.; Fina, A., Thermal conductivity of carbon nanotubes and their polymer nanocomposites: A review. *Progress in polymer science* **2011,** 36, (7), 914-944.

44. Min, C.; Shen, X.; Shi, Z.; Chen, L.; Xu, Z., The electrical properties and conducting mechanisms of carbon nanotube/polymer nanocomposites: A review. *Polymer-Plastics Technology and Engineering* **2010,** 49, (12), 1172-1181.

45. Yan, D. X.; Pang, H.; Li, B.; Vajtai, R.; Xu, L.; Ren, P. G.; Wang, J. H.; Li, Z. M., Structured reduced graphene oxide/polymer composites for ultra-efficient electromagnetic interference shielding. *Advanced Functional Materials* **2015,** 25, (4), 559-566.

46. Cui, Y.; Kundalwal, S.; Kumar, S., Gas barrier performance of graphene/polymer nanocomposites. *Carbon* **2016,** 98, 313-333.

47. Potts, J. R.; Dreyer, D. R.; Bielawski, C. W.; Ruoff, R. S., Graphene-based polymer nanocomposites. *Polymer* **2011,** 52, (1), 5-25.

48. Yu, X.; Cheng, H.; Zhang, M.; Zhao, Y.; Qu, L.; Shi, G., Graphene-based smart materials. *Nature Reviews Materials* **2017,** 2, (9), 1-13.

49. Moniruzzaman, M.; Winey, K. I., Polymer nanocomposites containing carbon nanotubes. *Macromolecules* **2006,** 39, (16), 5194-5205.

50. Kamal, M. R.; Khoshkava, V., Effect of cellulose nanocrystals (CNC) on rheological and mechanical properties and crystallization behavior of PLA/CNC nanocomposites. *Carbohydrate polymers* **2015,** 123, 105-114.

51. Wang, M. S.; Pinnavaia, T. J., Clay-polymer nanocomposites formed from acidic derivatives of montmorillonite and an epoxy resin. *Chemistry of Materials* **1994,** 6, (4), 468-474.

52. Etemadi, H. Silver Nanoparticles-Polymer Nanocomposites. University of Manchester, 2012.

53. Pérez-Juste, J.; Rodríguez-González, B.; Mulvaney, P.; Liz-Marzán, L. M., Optical control and patterning of gold-nanorod–poly (vinyl alcohol) nanocomposite films. *Advanced Functional Materials* **2005,** 15, (7), 1065-1071.

54. Geim, A. K.; Novoselov, K. S., The rise of graphene. In *Nanoscience and Technology: A Collection of Reviews from Nature Journals*, World Scientific: 2010; pp 11-19.

55. Geim, A. K., Graphene: status and prospects. *Science* **2009,** 324, (5934), 1530-1534.

56. Lee, C.; Wei, X.; Kysar, J. W.; Hone, J., Measurement of the elastic properties and intrinsic strength of monolayer graphene. *Science* **2008,** 321, (5887), 385-388.

57. Balandin, A. A., Thermal properties of graphene and nanostructured carbon materials. *Nature materials* **2011,** 10, (8), 569.

58. Castro, E. V.; Novoselov, K. S.; Morozov, S. V.; Peres, N.; Dos Santos, J. L.; Nilsson, J.; Guinea, F.; Geim, A.; Neto, A. C., Electronic properties of a biased graphene bilayer. *Journal of Physics: Condensed Matter* **2010,** 22, (17), 175503.

59. Dikin, D. A.; Stankovich, S.; Zimney, E. J.; Piner, R. D.; Dommett, G. H.; Evmenenko, G.; Nguyen, S. T.; Ruoff, R. S., Preparation and characterization of graphene oxide paper. *Nature* **2007,** 448, (7152), 457-460.

60. Zhu, Y.; Murali, S.; Cai, W.; Li, X.; Suk, J. W.; Potts, J. R.; Ruoff, R. S., Graphene and graphene oxide: synthesis, properties, and applications. *Advanced materials* **2010,** 22, (35), 3906-3924.

61. Compton, O. C.; Nguyen, S. T., Graphene oxide, highly reduced graphene oxide, and graphene: versatile building blocks for carbon-based materials. *small* **2010,** 6, (6), 711-723.

62. Seibers, Z.; Orr, M.; Collier, G. S.; Henriquez, A.; Gabel, M.; Shofner, M. L.; La Saponara, V.; Reynolds, J., Chemically Functionalized Reduced Graphene Oxide as Additives in Polyethylene Composites for Space Applications. *Polymer Engineering & Science* **2020,** 60, (1), 86-94.

63. Kausar, A.; Rafique, I.; Muhammad, B., Aerospace application of polymer nanocomposite with carbon nanotube, graphite, graphene oxide, and nanoclay. *Polymer-Plastics Technology and Engineering* **2017,** 56, (13), 1438-1456.

64. Naskar, A. K.; Keum, J. K.; Boeman, R. G., Polymer matrix nanocomposites for automotive structural components. *Nature nanotechnology* **2016,** 11, (12), 1026-1030.

65. Wang, W.; Xu, G.; Cui, X. T.; Sheng, G.; Luo, X., Enhanced catalytic and dopamine sensing properties of electrochemically reduced conducting polymer nanocomposite doped with pure graphene oxide. *Biosensors and Bioelectronics* **2014,** 58, 153-156.

66. Zhang, D.; Tong, J.; Xia, B., Humidity-sensing properties of chemically reduced graphene oxide/polymer nanocomposite film sensor based on layer-by-layer nano self-assembly. *Sensors and Actuators B: Chemical* **2014,** 197, 66-72.

67. Mishra, S. K.; Tripathi, S. N.; Choudhary, V.; Gupta, B. D., SPR based fibre optic ammonia gas sensor utilizing nanocomposite film of PMMA/reduced graphene oxide prepared by in situ polymerization. *Sensors and Actuators B: Chemical* **2014,** 199, 190-200.

68. Ghosh, T.; Basak, U.; Bairi, P.; Ghosh, R.; Pakhira, M.; Ball, R.; Biswas, B.; Chatterjee, D. P., Hierarchical Nanocomposites by Oligomer-Initiated Controlled Polymerization of Aniline on Graphene Oxide Sheets for Energy Storage. *ACS Applied Nano Materials* **2020,** 3, (2), 1693-1705.

69. Xu, J.; Wang, K.; Zu, S.-Z.; Han, B.-H.; Wei, Z., Hierarchical nanocomposites of polyaniline nanowire arrays on graphene oxide sheets with synergistic effect for energy storage. *ACS nano* **2010,** 4, (9), 5019-5026.

70. Huang, H.-D.; Ren, P.-G.; Chen, J.; Zhang, W.-Q.; Ji, X.; Li, Z.-M., High barrier graphene oxide nanosheet/poly (vinyl alcohol) nanocomposite films. *Journal of Membrane Science* **2012,** 409, 156-163.

71. Arfat, Y. A.; Ahmed, J.; Ejaz, M.; Mullah, M., Polylactide/graphene oxide nanosheets/clove essential oil composite films for potential food packaging applications. *International journal of biological macromolecules* **2018,** 107, 194-203.

72. Li, K.; Jin, S.; Li, J.; Chen, H., Improvement in antibacterial and functional properties of mussel-inspired cellulose nanofibrils/gelatin nanocomposites incorporated with graphene oxide for active packaging. *Industrial Crops and Products* **2019,** 132, 197-212.

73. Ghanem, A. F.; Youssef, A. M.; Rehim, M. H. A., Hydrophobically modified graphene oxide as a barrier and antibacterial agent for polystyrene packaging. *Journal of Materials Science* **2020,** 55, (11), 4685-4700.

74. Ruiz, S.; Tamayo, J. A.; Delgado Ospina, J.; Navia Porras, D. P.; Valencia Zapata, M. E.; Mina Hernandez, J. H.; Valencia, C. H.; Zuluaga, F.; Grande Tovar, C. D., Antimicrobial films based on nanocomposites of chitosan/poly (vinyl alcohol)/graphene oxide for biomedical applications. *Biomolecules* **2019,** 9, (3), 109.

75. Farshid, B.; Lalwani, G.; Mohammadi, M. S.; Sankaran, J. S.; Patel, S.; Judex, S.; Simonsen, J.; Sitharaman, B., Two-dimensional graphene oxide-reinforced porous biodegradable polymeric

nanocomposites for bone tissue engineering. *Journal of Biomedical Materials Research Part A* **2019,** 107, (6), 1143-1153.

76. Rikhari, B.; Mani, S. P.; Rajendran, N., Polypyrrole/graphene oxide composite coating on Ti implants: a promising material for biomedical applications. *Journal of Materials Science* **2020,** 55, (12), 5211-5229.

77. Yi, J.; Choe, G.; Park, J.; Lee, J. Y., Graphene oxide-incorporated hydrogels for biomedical applications. *Polymer Journal* **2020**, 1-15.

78. Kong, W.; Kum, H.; Bae, S.-H.; Shim, J.; Kim, H.; Kong, L.; Meng, Y.; Wang, K.; Kim, C.; Kim, J., Path towards graphene commercialization from lab to market. *Nature nanotechnology* **2019,** 14, (10), 927-938.

79. Facts, P. E. P. T., An analysis of European plastics production, demand and waste data. **2019**.

80. IEA, The future of petrochemicals. *Future Petrochemicals* **2018**.

81. Neufeld, L.; Stassen, F.; Sheppard, R.; Gilman, T. In *The new plastics economy: rethinking the future of plastics*, World Economic Forum, 2016; 2016.

82. Zhang, C.; Garrison, T. F.; Madbouly, S. A.; Kessler, M. R., Recent advances in vegetable oil-based polymers and their composites. *Progress in Polymer Science* **2017,** 71, 91-143.

83. Wang, Z.; Lu, X.; Sun, S.; Yu, C.; Xia, H., Preparation, characterization and properties of intrinsic self-healing elastomers. *Journal of Materials Chemistry B* **2019,** 7, (32), 4876-4926.

84. Deng, Z.; Wang, H.; Ma, P. X.; Guo, B., Self-healing conductive hydrogels: preparation, properties and applications. *Nanoscale* **2020**.

85. Yang, Y.; Urban, M. W., Self-healing polymeric materials. *Chemical Society Reviews* **2013,** 42, (17), 7446-7467.

86. Binder, W. H., *Self-healing polymers: from principles to applications*. John Wiley & Sons: 2013.

87. Bilodeau, R. A.; Kramer, R. K., Self-healing and damage resilience for soft robotics: a review. *Frontiers in Robotics and AI* **2017,** 4, 48.

88. Jony, B.; Roy, S.; Mulani, S. B., Fracture Resistance of In-Situ Healed CFRP Composite Using Thermoplastic Healants. *Materials Today Communications* **2020**, 101067.

89. Huebsch, N.; Kearney, C. J.; Zhao, X.; Kim, J.; Cezar, C. A.; Suo, Z.; Mooney, D. J., Ultrasound-triggered disruption and self-healing of reversibly cross-linked hydrogels for drug delivery and enhanced chemotherapy. *Proceedings of the National Academy of Sciences* **2014,** 111, (27), 9762-9767.

90. Yang, W. J.; Tao, X.; Zhao, T.; Weng, L.; Kang, E.-T.; Wang, L., Antifouling and antibacterial hydrogel coatings with self-healing properties based on a dynamic disulfide exchange reaction. *Polymer Chemistry* **2015,** 6, (39), 7027-7035.

91. Cho, S. H.; White, S. R.; Braun, P. V., Self-healing polymer coatings. *Advanced Materials* **2009,** 21, (6), 645-649.

92. Zhang, Z. P.; Rong, M. Z.; Zhang, M. Q., Polymer engineering based on reversible covalent chemistry: A promising innovative pathway towards new materials and new functionalities. *Progress in Polymer Science* **2018,** 80, 39-93.

93. Chakma, P.; Konkolewicz, D., Dynamic covalent bonds in polymeric materials. *Angewandte Chemie International Edition* **2019,** 58, (29), 9682-9695.

94. Terryn, S.; Brancart, J.; Lefeber, D.; Van Assche, G.; Vanderborght, B., Self-healing soft pneumatic robots. *Sci. Robot* **2017,** 2, (9), 1-12.

95. Bapat, A. P.; Sumerlin, B. S.; Sutti, A., Bulk network polymers with dynamic B–O bonds: healable and reprocessable materials. *Materials Horizons* **2020,** 7, (3), 694-714.

96. Chen, Y.; Guan, Z., Multivalent hydrogen bonding block copolymers self-assemble into strong and tough self-healing materials. *Chemical Communications* **2014,** 50, (74), 10868-10870.

97. Mei, J. F.; Jia, X. Y.; Lai, J. C.; Sun, Y.; Li, C. H.; Wu, J. H.; Cao, Y.; You, X. Z.; Bao, Z., A highly stretchable and autonomous self-healing polymer based on combination of pt···pt and π–π interactions. *Macromolecular rapid communications* **2016,** 37, (20), 1667-1675.

98. Hu, Z.; Zhang, D.; Lu, F.; Yuan, W.; Xu, X.; Zhang, Q.; Liu, H.; Shao, Q.; Guo, Z.; Huang, Y., Multistimuli-responsive intrinsic self-healing epoxy resin constructed by host–guest interactions. *Macromolecules* **2018,** 51, (14), 5294-5303.

99. Shi, L.; Ding, P.; Wang, Y.; Zhang, Y.; Ossipov, D.; Hilborn, J., Self-Healing Polymeric Hydrogel Formed by Metal–Ligand Coordination Assembly: Design, Fabrication, and Biomedical Applications. *Macromolecular rapid communications* **2019,** 40, (7), 1800837.

100. Rattanangkool, E.; Krailat, W.; Vilaivan, T.; Phuwapraisirisan, P.; Sukwattanasinitt, M.; Wacharasindhu, S., Hypervalent Iodine (III)-promoted metal-free S–H activation: an approach for the construction of S–S, S–N, and S–C bonds. *European Journal of Organic Chemistry* **2014,** 2014, (22), 4795-4804.

101. Machado, T. O.; Sayer, C.; Araujo, P. H., Thiol-ene polymerisation: a promising technique to obtain novel biomaterials. *European Polymer Journal* **2017,** 86, 200-215.

102. Lowe, A. B., Thiol-ene “click” reactions and recent applications in polymer and materials synthesis. *Polymer Chemistry* **2010,** 1, (1), 17-36.

103. Sirrine, J. M.; Meenakshisundaram, V.; Moon, N. G.; Scott, P. J.; Mondschein, R. J.; Weiseman, T. F.; Williams, C. B.; Long, T. E., Functional siloxanes with photo-activated, simultaneous chain extension and crosslinking for lithography-based 3D printing. *Polymer* **2018,** 152, 25-34.

104. Sirrine, J. M.; Zlatanic, A.; Meenakshisundaram, V.; Messman, J. M.; Williams, C. B.; Dvornic, P. R.; Long, T. E., 3D printing amorphous polysiloxane terpolymers via vat photopolymerization. *Macromolecular Chemistry and Physics* **2019,** 220, (4), 1800425.

105. Li, Z.; Wang, C.; Qiu, W.; Liu, R., Antimicrobial Thiol–ene–acrylate Photosensitive Resins for DLP 3D Printing. *Photochemistry and photobiology* **2019,** 95, (5), 1219-1229.

106. Zhao, T.; Yu, R.; Li, S.; Li, X.; Zhang, Y.; Yang, X.; Zhao, X.; Wang, C.; Liu, Z.; Dou, R., Superstretchable and Processable Silicone Elastomers by Digital Light Processing 3D Printing. *ACS applied materials & interfaces* **2019,** 11, (15), 14391-14398.

107. Bagheri, A.; Jin, J., Photopolymerization in 3D printing. *ACS Applied Polymer Materials* **2019,** 1, (4), 593-611.

108. Zhang, B.; Kowsari, K.; Serjouei, A.; Dunn, M. L.; Ge, Q., Reprocessable thermosets for sustainable three-dimensional printing. *Nature communications* **2018,** 9, (1), 1-7.

109. Arshad, M.; Saied, S.; Ullah, A., PEG–lipid telechelics incorporating fatty acids from canola oil: synthesis, characterization and solution self-assembly. *RSC advances* **2014,** 4, (50), 26439-26446.

110. Pradhan, R. A.; Arshad, M.; Ullah, A., Solvent-free rapid ethenolysis of fatty esters from spent hen and other lipidic feedstock with high turnover numbers. *Journal of Industrial and Engineering Chemistry* **2020,** 84, 42-45.

111. Maiti, B.; De, P., RAFT polymerization of fatty acid containing monomers: controlled synthesis of polymers from renewable resources. *RSC Advances* **2013,** 3, (47), 24983-24990.

112. Arshad, M.; Huang, L.; Ullah, A., Lipid-derived monomer and corresponding bio-based nanocomposites. *Polymer International* **2016,** 65, (6), 653-660.

113. Xiang, H.; Wang, X.; Ou, Z.; Lin, G.; Yin, J.; Liu, Z.; Zhang, L.; Liu, X., UV-curable, 3D printable and biocompatible silicone elastomers. *Progress in Organic Coatings* **2019,** 137, 105372.

114. Yang, X.; Guo, L.; Xu, X.; Shang, S.; Liu, H., A fully bio-based epoxy vitrimer: Self-healing, triple-shape memory and reprocessing triggered by dynamic covalent bond exchange. *Materials & Design* **2020,** 186, 108248.

115. Jin, L.; Geng, K.; Arshad, M.; Ahmadi, R.; Ullah, A., Synthesis of Fully Biobased Polyesters from Plant Oil. *ACS Sustainable Chemistry & Engineering* **2017,** 5, (11), 9793-9801.

116. Arshad, M.; Pradhan, R. A.; Ullah, A., Synthesis of lipid-based amphiphilic block copolymer and its evaluation as nano drug carrier. *Materials Science and Engineering: C* **2017,** 76, 217-223.

117. Ko, D.; Lee, J. S.; Patel, H. A.; Jakobsen, M. H.; Hwang, Y.; Yavuz, C. T.; Hansen, H. C. B.; Andersen, H. R., Selective removal of heavy metal ions by disulfide linked polymer networks. *Journal of hazardous materials* **2017,** 332, 140-148.

118. Ko, D.; Mines, P. D.; Jakobsen, M. H.; Yavuz, C. T.; Hansen, H. C. B.; Andersen, H. R., Disulfide polymer grafted porous carbon composites for heavy metal removal from stormwater runoff. *Chemical Engineering Journal* **2018,** 348, 685-692.

119. Rao, C.; Venkataraghavan, R.; Kasturi, T., Contribution to the infrared spectra of organosulphur compounds. *Canadian journal of chemistry* **1964,** 42, (1), 36-42.

120. Lowe, A. B., Thiol–ene "click" reactions and recent applications in polymer and materials synthesis: a first update. *Polymer Chemistry* **2014,** 5, (17), 4820-4870.

121. Khire, V. S.; Lee, T. Y.; Bowman, C. N., Surface modification using thiol− acrylate conjugate addition reactions. *Macromolecules* **2007,** 40, (16), 5669-5677.

122. Chan, J. W.; Hoyle, C. E.; Lowe, A. B.; Bowman, M., Nucleophile-initiated thiol-Michael reactions: effect of organocatalyst, thiol, and ene. *Macromolecules* **2010,** 43, (15), 6381-6388.

123. Nair, D. P.; Podgorski, M.; Chatani, S.; Gong, T.; Xi, W.; Fenoli, C. R.; Bowman, C. N., The thiol-Michael addition click reaction: a powerful and widely used tool in materials chemistry. *Chemistry of Materials* **2014,** 26, (1), 724-744.

124. Radl, S.; Schipfer, C.; Kaiser, S.; Moser, A.; Kaynak, B.; Kern, W.; Schlögl, S., Photo-responsive thiol–ene networks for the design of switchable polymer patterns. *Polymer Chemistry* **2017,** 8, (9), 1562-1572.

125. Chakma, P.; Digby, Z. A.; Via, J.; Shulman, M. P.; Sparks, J. L.; Konkolewicz, D., Tuning thermoresponsive network materials through macromolecular architecture and dynamic thiol-Michael chemistry. *Polymer Chemistry* **2018,** 9, (38), 4744-4756.

126. Bowman, C. N.; Nair, D. P.; Podgorski, M.; Chatani, S., Thiol-containing dual cure polymers and methods using same. In Google Patents: 2016.

127. Gao, Y.; Wang, J.; Liang, X.; Yan, Z.; Liu, Y.; Cai, Y., Investigation on permeation properties of liquids into HTV silicone rubber materials. *IEEE Transactions on Dielectrics and Electrical Insulation* **2014,** 21, (6), 2428-2437.

128. Mekaru, H.; Yoshigoe, A.; Nakamura, M.; Doura, T.; Tamanoi, F., Biodegradability of Disulfide-Organosilica Nanoparticles Evaluated by Soft X-ray Photoelectron Spectroscopy: Cancer Therapy Implications. *ACS Applied Nano Materials* **2018,** 2, (1), 479-488.

129. Hoque, M.; Zhang, S.; Thomas, M. L.; Li, Z.; Suzuki, S.; Ando, A.; Yanagi, M.; Kobayashi, Y.; Dokko, K.; Watanabe, M., Simple combination of a protic salt and an iron halide: precursor for a Fe, N and S co-doped catalyst for the oxygen reduction reaction in alkaline and acidic media. *Journal of Materials Chemistry A* **2018,** 6, (3), 1138-1149.

130. Yang, W. J.; Neoh, K.-G.; Kang, E.-T.; Teo, S. L.-M.; Rittschof, D., Stainless steel surfaces with thiol-terminated hyperbranched polymers for functionalization via thiol-based chemistry. *Polymer Chemistry* **2013,** 4, (10), 3105-3115.

131. Li, Y.; Wu, K.-H.; Huang, N.; Dalapati, S.; Su, B.-J.; Jang, L.-Y.; Gentle, I. R.; Jiang, D.; Wang, D.-W., Long-chain solid organic polysulfide cathode for high-capacity secondary lithium batteries. *Energy Storage Materials* **2018,** 12, 30-36.

132. Mueller, J.; Shea, K.; Daraio, C., Mechanical properties of parts fabricated with inkjet 3D printing through efficient experimental design. *Materials & Design* **2015,** 86, 902-912.

133. Mostafa, K. G.; Arshad, M.; Ullah, A.; Nobes, D. S.; Qureshi, A. J., Concurrent Modelling and Experimental Investigation of Material Properties and Geometries Produced by Projection Microstereolithography. *Polymers* **2020,** 12, (3), 506.

134. De Gans, B. J.; Duineveld, P. C.; Schubert, U. S., Inkjet printing of polymers: state of the art and future developments. *Advanced materials* **2004,** 16, (3), 203-213.

135. Caraballo, R.; Rahm, M.; Vongvilai, P.; Brinck, T.; Ramström, O., Phosphine-catalyzed disulfide metathesis. *Chemical communications* **2008**, (48), 6603-6605.

136. Furusho, Y.; Oku, T.; Hasegawa, T.; Tsuboi, A.; Kihara, N.; Takata, T., Dynamic Covalent Approach to [2]-and [3] Rotaxanes by Utilizing a Reversible Thiol–Disulfide Interchange Reaction. *Chemistry–A European Journal* **2003,** 9, (12), 2895-2903.

137. Fernandes, P. A.; Ramos, M. J., Theoretical insights into the mechanism for thiol/disulfide exchange. *Chemistry–A European Journal* **2004,** 10, (1), 257-266.

138. Pepels, M.; Filot, I.; Klumperman, B.; Goossens, H., Self-healing systems based on disulfide–thiol exchange reactions. *Polymer Chemistry* **2013,** 4, (18), 4955-4965.

139. Yoon, J. A.; Kamada, J.; Koynov, K.; Mohin, J.; Nicolaÿ, R.; Zhang, Y.; Balazs, A. C.; Kowalewski, T.; Matyjaszewski, K., Self-healing polymer films based on thiol–disulfide exchange reactions and self-healing kinetics measured using atomic force microscopy. *Macromolecules* **2012,** 45, (1), 142-149.

140. Chandrasiri, J. A.; Wilkie, C. A., Thermal degradation of diphenyl disulfide and a blend of diphenyl disulfide with poly (methyl methacrylate). *Polymer degradation and stability* **1994,** 46, (2), 275-284.

141. Jiang, D. D.; Yao, Q.; McKinney, M. A.; Wilkie, C. A., TGA/FTIR studies on the thermal degradation of some polymeric sulfonic and phosphonic acids and their sodium salts. *Polymer degradation and stability* **1999,** 63, (3), 423-434.

142. Bunch, J. S.; Verbridge, S. S.; Alden, J. S.; Van Der Zande, A. M.; Parpia, J. M.; Craighead, H. G.; McEuen, P. L., Impermeable atomic membranes from graphene sheets. *Nano letters* **2008,** 8, (8), 2458-2462.

143. Stoller, M. D.; Park, S.; Zhu, Y.; An, J.; Ruoff, R. S., Graphene-based ultracapacitors. *Nano letters* **2008,** 8, (10), 3498-3502.

144. Kim, H.; Abdala, A. A.; Macosko, C. W., Graphene/polymer nanocomposites. *Macromolecules* **2010,** 43, (16), 6515-6530.

145. Zhang, L.; Tu, S.; Wang, H.; Du, Q., Preparation of polymer/graphene oxide nanocomposites by a two-step strategy composed of in situ polymerization and melt processing. *Composites Science and Technology* **2018,** 154, 1-7.

146. Sandhya, P.; Sreekala, M.; Padmanabhan, M.; Jesitha, K.; Thomas, S., Effect of starch reduced graphene oxide on thermal and mechanical properties of phenol formaldehyde resin nanocomposites. *Composites Part B: Engineering* **2019,** 167, 83-92.

147. Tsagkalias, I.; Manios, T.; Achilias, D., Effect of Graphene Oxide on the Reaction Kinetics of Methyl Methacrylate In Situ Radical Polymerization via the Bulk or Solution Technique. *Polymers* **2017,** 9, (9), 432.

148. Xu, Y.; Hong, W.; Bai, H.; Li, C.; Shi, G., Strong and ductile poly (vinyl alcohol)/graphene oxide composite films with a layered structure. *Carbon* **2009,** 47, (15), 3538-3543.

149. Cobos, M.; De-La-Pinta, I.; Quindós, G.; Fernández, M. J.; Fernández, M. D., One-step eco-friendly synthesized silver-graphene oxide/poly (vinyl alcohol) antibacterial nanocomposites. *Carbon* **2019,** 150, 101-116.

150. Bortz, D. R.; Heras, E. G.; Martin-Gullon, I., Impressive fatigue life and fracture toughness improvements in graphene oxide/epoxy composites. *Macromolecules* **2011,** 45, (1), 238-245.

151. Potts, J. R.; Shankar, O.; Du, L.; Ruoff, R. S., Processing–morphology–property relationships and composite theory analysis of reduced graphene oxide/natural rubber nanocomposites. *Macromolecules* **2012,** 45, (15), 6045-6055.

152. Wang, J.; Jin, X.; Li, C.; Wang, W.; Wu, H.; Guo, S., Graphene and graphene derivatives toughening polymers: Toward high toughness and strength. *Chemical Engineering Journal* **2019**.

153. Ye, S.; Cao, Y.; Feng, J.; Wu, P., Temperature-dependent compatibilizing effect of graphene oxide as a compatibilizer for immiscible polymer blends. *Rsc Advances* **2013,** 3, (21), 7987-7995.

154. Mao, C.; Zhu, Y.; Jiang, W., Design of electrical conductive composites: tuning the morphology to improve the electrical properties of graphene filled immiscible polymer blends. *ACS applied materials & interfaces* **2012,** 4, (10), 5281-5286.

155. Kim, H.; Miura, Y.; Macosko, C. W., Graphene/polyurethane nanocomposites for improved gas barrier and electrical conductivity. *Chemistry of materials* **2010,** 22, (11), 3441-3450.

156. Gelfer, M. Y.; Song, H. H.; Liu, L.; Hsiao, B. S.; Chu, B.; Rafailovich, M.; Si, M.; Zaitsev, V., Effects of organoclays on morphology and thermal and rheological properties of polystyrene and poly (methyl methacrylate) blends. *Journal of Polymer Science Part B: Polymer Physics* **2003,** 41, (1), 44-54.

157. Sultana, S. N.; Pawar, S. P.; Sundararaj, U., Effect of Processing Techniques on EMI SE of Immiscible PS/PMMA Blends Containing MWCNT: Enhanced Intertube and Interphase Scattering. *Industrial & Engineering Chemistry Research* **2019**.

158. Mayo, J. D.; Behal, S.; Adronov, A., Phase separation of polymer-functionalized SWNTs within a PMMA/polystyrene blend. *Journal of Polymer Science Part A: Polymer Chemistry* **2009,** 47, (2), 450-458.

159. Marcano, D. C.; Kosynkin, D. V.; Berlin, J. M.; Sinitskii, A.; Sun, Z.; Slesarev, A.; Alemany, L. B.; Lu, W.; Tour, J. M., Improved synthesis of graphene oxide. *ACS nano* **2010,** 4, (8), 4806-4814.

160. Monteserín, C.; Blanco, M.; Aranzabe, E.; Aranzabe, A.; Laza, J. M.; Larrañaga-Varga, A.; Vilas, J. L., Effects of graphene oxide and chemically-reduced graphene oxide on the dynamic mechanical properties of epoxy amine composites. *Polymers* **2017,** 9, (9), 449.

161. Krishnamoorthy, K.; Veerapandian, M.; Yun, K.; Kim, S.-J., The chemical and structural analysis of graphene oxide with different degrees of oxidation. *Carbon* **2013,** 53, 38-49.

162. Matusinović, Z.; Rogošić, M.; Šipušić, J., Synthesis and characterization of poly (styrene-co-methyl methacrylate)/layered double hydroxide nanocomposites via in situ polymerization. *Polymer degradation and stability* **2009,** 94, (1), 95-101.

163. Sahoo, G.; Sarkar, N.; Sahu, D.; Swain, S. K., Nano gold decorated reduced graphene oxide wrapped polymethylmethacrylate for supercapacitor applications. *RSC Advances* **2017,** 7, (4), 2137-2150.

164. Fu, S.; Sun, Z.; Huang, P.; Li, Y.; Hu, N., Some basic aspects of polymer nanocomposites: A critical review. *Nano Materials Science* **2019,** 1, (1), 2-30.

165. Potts, J. R.; Lee, S. H.; Alam, T. M.; An, J.; Stoller, M. D.; Piner, R. D.; Ruoff, R. S., Thermomechanical properties of chemically modified graphene/poly (methyl methacrylate) composites made by in situ polymerization. *Carbon* **2011,** 49, (8), 2615-2623.

166. Kim, H.; Macosko, C. W., Morphology and properties of polyester/exfoliated graphite nanocomposites. *Macromolecules* **2008,** 41, (9), 3317-3327.

167. Matos, C. F.; Galembeck, F.; Zarbin, A. J., Multifunctional and environmentally friendly nanocomposites between natural rubber and graphene or graphene oxide. *Carbon* **2014,** 78, 469-479.

168. Ton-That, C.; Shard, A.; Teare, D.; Bradley, R., XPS and AFM surface studies of solvent-cast PS/PMMA blends. *Polymer* **2001,** 42, (3), 1121-1129.

169. Ramanathan, T.; Abdala, A.; Stankovich, S.; Dikin, D.; Herrera-Alonso, M.; Piner, R. D.; Adamson, D.; Schniepp, H.; Chen, X.; Ruoff, R., Functionalized graphene sheets for polymer nanocomposites. *Nature nanotechnology* **2008,** 3, (6), 327.

170. Shin, M. K.; Lee, B.; Kim, S. H.; Lee, J. A.; Spinks, G. M.; Gambhir, S.; Wallace, G. G.; Kozlov, M. E.; Baughman, R. H.; Kim, S. J., Synergistic toughening of composite fibres by self-alignment of reduced graphene oxide and carbon nanotubes. *Nature communications* **2012,** 3, 650.

171. Tang, L.-C.; Wan, Y.-J.; Yan, D.; Pei, Y.-B.; Zhao, L.; Li, Y.-B.; Wu, L.-B.; Jiang, J.-X.; Lai, G.-Q., The effect of graphene dispersion on the mechanical properties of graphene/epoxy composites. *Carbon* **2013,** 60, 16-27.

172. Wang, J.; Li, C.; Zhang, X.; Xia, L.; Zhang, X.; Wu, H.; Guo, S., Polycarbonate toughening with reduced graphene oxide: Toward high toughness, strength and notch resistance. *Chemical Engineering Journal* **2017,** 325, 474-484.

173. Ritchie, R. O., The conflicts between strength and toughness. *Nature materials* **2011,** 10, (11), 817.

174. Liang, J.; Huang, Y.; Zhang, L.; Wang, Y.; Ma, Y.; Guo, T.; Chen, Y., Molecular-level dispersion of graphene into poly (vinyl alcohol) and effective reinforcement of their nanocomposites. *Advanced Functional Materials* **2009,** 19, (14), 2297-2302.

175. Peña-Bahamonde, J.; San-Miguel, V.; Baselga, J.; Fernández-Blázquez, J. P.; Gedler, G.; Ozisik, R.; Cabanelas, J. C., Effect of polysulfone brush functionalization on thermo-mechanical properties of melt extruded graphene/polysulfone nanocomposites. *Carbon* **2019,** 151, 84-93.

176. Gómez-Navarro, C.; Burghard, M.; Kern, K., Elastic properties of chemically derived single graphene sheets. *Nano letters* **2008,** 8, (7), 2045-2049.

177. Fan, J.; Shi, Z.; Zhang, L.; Wang, J.; Yin, J., Aramid nanofiber-functionalized graphene nanosheets for polymer reinforcement. *Nanoscale* **2012,** 4, (22), 7046-7055.

178. TK, B. S.; Nair, A. B.; Abraham, B. T.; Beegum, P. S.; Thachil, E. T., Microwave exfoliated reduced graphene oxide epoxy nanocomposites for high performance applications. *Polymer* **2014,** 55, (16), 3614-3627.

179. Vadukumpully, S.; Paul, J.; Mahanta, N.; Valiyaveettil, S., Flexible conductive graphene/poly (vinyl chloride) composite thin films with high mechanical strength and thermal stability. *Carbon* **2011,** 49, (1), 198-205.

180. Wan, Y.-J.; Tang, L.-C.; Gong, L.-X.; Yan, D.; Li, Y.-B.; Wu, L.-B.; Jiang, J.-X.; Lai, G.-Q., Grafting of epoxy chains onto graphene oxide for epoxy composites with improved mechanical and thermal properties. *Carbon* **2014,** 69, 467-480.

181. Jiang, S.; Gui, Z.; Bao, C.; Dai, K.; Wang, X.; Zhou, K.; Shi, Y.; Lo, S.; Hu, Y., Preparation of functionalized graphene by simultaneous reduction and surface modification and its polymethyl methacrylate composites through latex technology and melt blending. *Chemical engineering journal* **2013,** 226, 326-335.